

A QUANTITATIVE TEST OF THE NO-HAIR THEOREM WITH Sgr A* USING STARS, PULSARS, AND THE EVENT HORIZON TELESCOPE

DIMITRIOS PSALTIS¹, NORBERT WEX², MICHAEL KRAMER²

¹Astronomy Department, University of Arizona, 933 North Cherry Avenue, Tucson, AZ 85721, USA and

²Max-Planck-Institut für Radioastronomie, Auf dem Hügel 69, 53121, Bonn, Germany

Draft version August 22, 2018

ABSTRACT

The black hole in the center of the Milky Way, Sgr A*, has the largest mass-to-distance ratio among all known black holes in the Universe. This property makes Sgr A* the optimal target for testing the gravitational no-hair theorem. In the near future, major developments in instrumentation will provide the tools for high-precision studies of its spacetime via observations of relativistic effects in stellar orbits, in the timing of pulsars, and in horizon-scale images of its accretion flow. We explore here the prospect of measuring the properties of the black-hole spacetime using all these three types of observations. We show that the correlated uncertainties in the measurements of the black-hole spin and quadrupole moment using the orbits of stars and pulsars are nearly orthogonal to those obtained from measuring the shape and size of the shadow the black hole casts on the surrounding emission. Combining these three types of observations will, therefore, allow us to assess and quantify systematic biases and uncertainties in each measurement and lead to a highly accurate, quantitative test of the gravitational no-hair theorem.

Subject headings: black hole physics; gravitation; Galaxy: center; stars:general; pulsars:general

1. INTRODUCTION

One of the outstanding challenges in studying theories of gravity is the experimental verification of the existence of black holes and the measurement of their fundamental properties. Based on observational data, it is generally accepted that at least two types of astrophysical black holes can be identified, namely stellar-mass black holes with masses of several M_{\odot} (see Özel et al. 2010 for a recent compilation) and supermassive black holes with masses between 10^6 and $10^{10}M_{\odot}$ (see Ho 2008 for a review), where $M_{\odot} = 2 \times 10^{30}$ kg is the mass of the Sun.

While supermassive black holes are expected at the centers of most, if not, all galaxies, in both stellar and supermassive types most of the observational evidence is based on the interpretation of phenomena associated with accretion processes onto a compact object that lacks a hard surface (see, e.g., Narayan & McClintock 2013). At the same time, observations of the (gas or stellar) dynamics around unseen central objects often safely point to massive objects that are smaller than the Schwarzschild radius $R_{\bullet} = 2GM_{\bullet}/c^2 \sim 3 \text{ km } (M_{\bullet}/M_{\odot})$, where G is the gravitational constant and c is the speed of light.

Within general relativity (GR), R_{\bullet} is the equatorial circumferential radius of the event horizon of an uncharged black hole, i.e., the boundary in spacetime beyond which events cannot affect an outside observer. The requirement of an event horizon surrounding every singularity is trivial to prove for the case of an uncharged, spherically symmetric spacetime (e.g., the Birkhoff theorem) but has only been postulated for the most general case in the *Cosmic Censorship Conjecture* (Penrose 1979), which provides the means to separate the central singularity from the outside world.

In astrophysical situations, black holes are believed to be (practically) free of any net electrical charge but

not without angular momentum, i.e., black holes are expected to have spin. In this case, within GR, the outer spacetime is described by the Kerr metric¹, which exhibits an event horizon only for spins less than a maximum value. The cosmic censorship conjecture hence requires for the spin angular momentum S_{\bullet} of the black hole that

$$\chi \equiv \frac{c}{G} \frac{S_{\bullet}}{M_{\bullet}^2} \leq 1. \quad (1)$$

Astrophysical black holes are also expected to be the result of gravitational collapse of a progenitor and subsequent mass accretion from the surrounding medium. During the collapse and accretion phases, all the properties of the incoming material, apart from mass and spin, are radiated away by gravitational radiation while the gravitational field approaches exponentially its stationary configuration (Price 1972a,b). Indeed, a powerful uniqueness theorem within GR has been proven according to which all stationary, axisymmetric, vacuum spacetimes with no closed time-like loops and no pathologies outside their horizons are characterized by only three parameters: the mass (M_{\bullet}), the spin (S_{\bullet}), and the electric charge (“black holes have no hair”; Israel 1967,1968; Carter 1971; Hawking 1972; Robinson 1975).

A direct consequence of this no-hair theorem is that all high multipole moments ($l \geq 2$) of the gravitational field of a non-charged astrophysical black hole in GR can be expressed as a function of only M_{\bullet} and S_{\bullet} (Hansen 1974). In particular the quadrupole moment, Q_{\bullet} , which is the lowest-order moment that will be measured obser-

¹ Strictly speaking, this is only true within a certain approximation since, to some extent, astrophysical black holes will be influenced by nearby masses (accreting matter, orbiting objects, etc.)

vationally, fulfills the relation (Thorne 1980)

$$q \equiv \frac{c^4}{G^2} \frac{Q_\bullet}{M_\bullet^3} = -\chi^2. \quad (2)$$

One way of testing the uniqueness of black holes within GR, i.e., the Kerr hypothesis, and hence the properties of the strongly-curved spacetime around (spinning) black holes is to measure the mass, spin, and quadrupole moment of an astrophysical black hole and verify or refute the above relationship (Ryan 1995).

The cosmic censorship conjecture and the no-hair theorem address only a rather limited aspect of strong-field gravity: the asymptotic, non-dynamical configuration of vacuum gravitational fields (see discussion in Barausse & Sotiriou 2008). Verifying them observationally, however, will increase our confidence in our ability to use GR in order to predict the outcomes of more general strong-field gravitational experiments. Perhaps more exciting is the possibility that either the cosmic censorship conjecture or the no-hair theorem may be proven not to be satisfied for astrophysical black holes. Even though violating either or both can be accommodated, in principle, within GR, such an observational result will most likely have very serious consequences for the foundations of the theory. This is especially true since many minimal modifications of the gravity theory leave the no-hair theorem and the Kerr metric unaffected (see Psaltis et al. 2008; Sotiriou & Faraoni 2012).

The black hole in the center of our Galaxy provides the optimal setting for testing the cosmic conjecture hypothesis and the no-hair theorem with multiple, independent experimental probes (see Psaltis & Johannsen 2011 for an early discussion and Ghasemi-Nodehi et al. 2015). Optical/IR imaging of the stars in the central region revealed closed orbits around a central black hole with a mass of about $4.3 \times 10^6 M_\odot$ (Ghez et al. 2008; Gillessen et al. 2009a). At a distance of about 8.3 kpc, the implied apparent size of the shadow cast by the black hole on the surrounding emission is in the realm of Very Long Baseline Interferometry (VLBI) observations at mm-wavelengths (see Falcke et al. 2000).

An international effort is underway to conduct such a mm VLBI experiment with the Event Horizon Telescope (EHT) that will allow us to image the shadow of this supermassive black hole, known as Sagittarius A* (Sgr A*), against the background of emission from a hot accretion disk (Doeleman et al. 2009b). Initial EHT observations with only a minimal set of interferometric baselines have indeed confirmed the presence of horizon-scale structures in its emission, and simulations of the full array indicate that true imaging of strong-field general relativistic signatures will soon be possible (Fish et al 2014). Measuring the shape and size of the black-hole shadow can be used to infer the mass, quadrupole moment, and (to a lesser extent) the spin of the black hole and, hence, to test the cosmic conjecture hypothesis and the no-hair theorem (see, e.g., Bambi & Freese 2009; Johannsen & Psaltis 2010b; Broderick et al. 2014; Psaltis et al. 2015b).

The shape of the black-hole shadow is determined by purely gravitational effects and modeling it does not depend on our understanding of the accretion flow properties. Even though astrophysical effects, such as the presence of opaque plasma in front of the black hole,

might obscure partially the shadow, they will not affect its shape or size. As such, a test of the no-hair theorem with the EHT is largely immune to the usual complexities that are inherent in most astrophysical observations. However, there remains the possibility of systematic biases in such a measurement caused, e.g., by the misidentification of the outline of the black-hole shadow or by an erroneous subtraction of the blurring effects of interstellar scattering (Psaltis et al. 2015b; see also Fish et al. 2014; Lu et al. 2014).

The good news is that, in the near future, the spacetime of Sgr A* will be studied in more than one way, at a range of distances and with different probes by tracing the orbits of stars and pulsars with next generation instruments. For the former, the adaptive-optics assisted optical interferometer GRAVITY will have the ability to observe relativistic effects in the orbits of stars that reach within a few hundred gravitational radii of the central black hole (Eisenhauer et al. 2011). The power of the latter is derived from pulsar timing observations where, even for pulsars with relatively poor timing accuracy, the instantaneous time-of-arrival (TOA) for a pulsar signal can be measured with an uncertainty of a few hundred microseconds, corresponding to a light-travel (“ranging”) distance of only $\sim 10 - 100$ km. A phase-connected solution with an appropriate timing model leads to a determination of the pulsar orbit, which is considerably better than that. Hence, as argued by Wex & Kopeikin (1999), Pfahl & Loeb (2004) and Liu et al. (2012), a pulsar in orbit around the super-massive black hole in the Galactic Center would be a sensitive probe to the black-hole properties. A number of international projects are contributing to the EHT effort, the ERC-funded project BlackHoleCam among them, to exploit the synergy between probing the properties of Sgr A* using EHT imaging, stellar orbits, and pulsar timing.

The motivation of the work presented here is to demonstrate the power of combining the constraints derived from the EHT observations of the black-hole shadow to those from independent measurements based on stellar and pulsar orbits in quantifying and assessing potential systematic effects in the test of the no-hair theorem. In the following we describe the methods for the various experiments and their prospects, and demonstrate the synergies of the different approaches. After a general description of the Galactic Center black hole and its environment for stellar and pulsar orbits, we look at the possibility of probing the black-hole spacetime with stellar orbits. We then review and expand on the treatment of pulsar orbits, before we show how to combine the results of the previous sections with potential information from the imaging observations of Sgr A*.

2. GENERAL DEFINITIONS AND CONSIDERATIONS

2.1. *The Central Black Hole*

Optical/IR observations of the orbits of stars in the vicinity of Sgr A* have led to a measurement of its mass, M_\bullet , and distance from the Earth, D . The uncertainties in the two measurements are significant and highly correlated (Ghez et al. 2008; Gillessen et al. 2009). Because of the directions of these correlations, however, the uncertainty in the apparent size of the black-hole shadow, which is the most relevant quantity for the EHT observa-

tions, is significantly smaller. In the following discussion, we set the mass of Sgr A* to $M_{\bullet} = 4.3 \times 10^6 M_{\odot}$ and its distance to $D = 8.3$ kpc (Reid et al. 2014), such that the apparent opening angle of one gravitational radius (GM_{\bullet}/c^2) at the distance of Sgr A* is equal to $5.1 \mu\text{as}$ and consistent with the most likely value derived from current observations (Psaltis et al. 2015b).

Because of the large orbital distances of the currently known optical/IR stars around Sgr A*, there have been no dynamical measurements of its spin magnitude, χ , or orientation. Comparison of accretion flow models with spectroscopic and EHT imaging observations indicate low spins, when semi-analytic models are used (e.g., Broderick et al. 2011), or relatively high spins when GRMHD models are used (e.g., Dexter et al. 2010; Chan et al. 2015). Moreover, the small inferred size of the 1.3 mm image of Sgr A* supports the assumption that the black-hole spin is inclined by $\simeq 50 - 60^\circ$ with respect to the line of sight and is aligned with the angular momentum vector of the stellar disk at ~ 3 arcsec away from the black hole (Psaltis et al. 2015a). For the purposes of the present paper, we set the spin of Sgr A* to $\chi = 0.6$, which corresponds to a Kerr quadrupole moment of $q = -0.36$. We picked these values such that the effects of both the spin and of the quadrupole moment are potentially observable, without being maximal. Clearly, we can perform tests of the no-hair theorem only if the black hole in the center of the Milky Way is spinning.

2.2. The Inner Cluster of Stellar-Mass Objects

Advances in adaptive optics have revealed a large number of stars in orbit around Sgr A* (see Genzel et al. 2010; Ghez et al. 2012). One of these stars has been followed for at least one fully closed orbit (Ghez et al. 2008; Gillessen et al. 2009b) and the orbital parameters of several others (S0-16, S0-102, and S0-104) will eventually place them within a few thousand gravitational radii from the black hole (e.g., Meyer et al. 2012). Even though monitoring of these orbits in the near future will most likely lead to detection of periastron precession, additional relativistic effects that will allow for a test of the no hair theorem will either be too small to be detected or masked by other astrophysical complexities.

It is expected that observations with future instruments, such as the adaptive-optics assisted interferometer GRAVITY on the VLT (Eisenhauer et al. 2011) and new generation adaptive optics instruments on a 30-m class telescope (Weinberg et al. 2005), will lead to the discovery of stars with closer orbits. Monitoring the precession of their orbits and of their orbital planes will offer the possibility of measuring the spin and the quadrupole moment of the black hole and, therefore, of testing the no-hair theorem (Will 2008).

The distribution of stellar-mass objects within a few thousand gravitational radii from Sgr A* is very difficult to infer observationally at this point (see the detailed discussion in Merritt 2010). For the purposes of the current study, we will follow Merritt et al. (2010) and set the distribution of the semi-major orbital axes of stellar objects around the black hole such that

$$n(a) = \frac{N_0}{a_0^3} \left(\frac{a}{a_0} \right)^{-\gamma}. \quad (3)$$

We will write our expressions in the general case of $\gamma < 3$, but evaluate them in the corresponding figures for $\gamma = 2$ (Merritt et al. 2010) and $\gamma = 7/4$ (Bahcall & Wolf 1976), to quantify the effect of this assumed parameter. Requiring that the total mass of stars inside the characteristic orbital separation a_0 is equal to M_* , i.e.,

$$m_* \int_0^{a_0} 4\pi a^2 n(a) da = M_*, \quad (4)$$

we obtain for the normalization constant

$$N_0 = \frac{3 - \gamma}{4\pi} \frac{M_*}{m_*} \quad (5)$$

and for the total number of stars inside an orbit with semi-major axis a

$$N(a) = \left(\frac{a}{a_0} \right)^{3-\gamma} \frac{M_*}{m_*}. \quad (6)$$

The characteristic values for the mass m_* of each object and the total mass M_* enclosed inside an orbital separation a_0 are also poorly constrained from current observations. We will adopt here a conservative set of values (Merritt et al. 2010) for which $m_* = 1 M_{\odot}$, $a_0 = 1$ pc, and $M_* = 10^6 M_{\odot}$.

We can use this distribution to calculate the mass, angular momentum, and quadrupole moment due to the stellar cluster that is enclosed inside an orbit of a given semi-major axis. The ratio of these quantities to the black-hole mass, angular momentum, and quadrupole moment will represent the limiting accuracies to which these black-hole properties can be inferred using observations of orbits of stars and pulsars.

The mass of stars inside a circular orbit with semi-major axis a

$$M_*(a) = m_* \int_0^a 4\pi a^2 n(a) da \quad (7)$$

and the relative contribution to the mass of the black hole is

$$\begin{aligned} \frac{M_*(a)}{M_{\bullet}} &= \left(\frac{M_*}{M_{\bullet}} \right) \left(\frac{a}{a_0} \right)^{3-\gamma} \\ &= 4.8 \times 10^{-8} \left(\frac{M_*}{10^6 M_{\odot}} \right) \left(\frac{a_0}{1 \text{ pc}} \right)^{-1} \left(\frac{ac^2}{GM_{\bullet}} \right) \end{aligned} \quad (8)$$

where in the last expression we set $\gamma = 2$.

The enclosed angular momentum due to the stellar cluster depends on the relative orientation of the orbits and the distribution of their eccentricities. We can obtain an upper limit to the enclosed angular momentum by assuming that all orbits are circular and aligned. In this case, the enclosed angular momentum is

$$J_*(a) = m_* \int_0^a 4\pi a^2 n(a) (GM_{\bullet} a)^{1/2} da. \quad (9)$$

The dimensional spin angular momentum of the black hole is $S_{\bullet} \equiv \chi GM_{\bullet}^2/c$ (cf. equation [1]) and, hence, the magnitude of the relative contribution to the angular momentum due to the stellar cluster is

$$\chi \frac{J_*(a)}{S_{\bullet}} = \frac{2(3-\gamma)}{7-2\gamma} \left(\frac{a}{a_0} \right)^{3-\gamma} \left(\frac{M_*}{M_{\bullet}} \right) \left(\frac{ac^2}{GM_{\bullet}} \right)^{1/2}$$

$$= 3 \times 10^{-8} \left(\frac{M_*}{10^6 M_\odot} \right) \left(\frac{a_0}{1 \text{ pc}} \right)^{-1} \left(\frac{ac^2}{GM_\bullet} \right)^{3/2}, \quad (10)$$

where in the last expression we set $\gamma = 2$.

The enclosed quadrupole moment due to the stellar cluster also depends on the orientation of the orbits. If we add an axisymmetric angular dependence to the distribution of orbits, i.e., denote this distribution by $n(a, \theta, \phi) = n(a)n_\theta(\theta)$, then the quadrupole mass moment of the stellar cluster becomes

$$\begin{aligned} Q_*(a) &= \frac{m_*}{2} \int_0^a a^2 n(a, \theta, \phi) (3 \cos^2 \theta - 1) a^2 da d\phi d \cos \theta \\ &= \frac{\tilde{n}_\theta}{12} \left(\frac{a}{a_0} \right) M_* a^2, \end{aligned} \quad (11)$$

where we have defined

$$\tilde{n}_\theta \equiv \int_{-1}^1 (3 \cos^2 \theta - 1) n_\theta(\theta) d \cos \theta. \quad (12)$$

The dimensional quadrupole angular momentum of the black hole is $Q_\bullet = q G^2 M_\bullet^3 / c^4$ (cf. equation [2]) and, hence, the magnitude of the relative contribution to the quadrupole moment due to the stellar cluster is

$$\begin{aligned} q \frac{Q_*(a)}{Q_\bullet} &= \frac{(3 - \gamma) \tilde{n}_\theta}{4(5 - \gamma)} \left(\frac{M_*}{M_\bullet} \right) \left(\frac{a}{a_0} \right)^{3 - \gamma} \left(\frac{ac^2}{GM_\bullet} \right)^2 \\ &= 4.0 \times 10^{-10} \left(\frac{\tilde{n}_\theta}{0.1} \right) \left(\frac{M_*}{10^6 M_\odot} \right) \left(\frac{a_0}{1 \text{ pc}} \right)^{-1} \\ &\quad \left(\frac{ac^2}{GM_\bullet} \right)^3, \end{aligned} \quad (13)$$

where in the last expression we set $\gamma = 2$.

The fractional contributions to the mass, angular momentum, and quadrupole moment enclosed inside an orbit of semi-major axis a are shown in Figure 1. Our goal is to use orbits of stars and pulsars to measure the quadrupole moment of the black hole and test the no-hair theorem. Just imposing the requirement that the stellar cluster does not dominate the quadrupole moment of the gravitational field forces us to use circular orbits with orbital separations (or equivalently elliptical orbits with periapsis distances) that are inside a few times $\simeq 1000 GM_\bullet / c^2$ (see also Merritt et al. 2010). For pulsars in highly eccentric orbits ($e \gtrsim 0.8$), as we will demonstrate in Section 4, we have, besides the secular precession of the orbit, an additional probe of the relativistic effects via the near-periapsis periodic contributions, which are less affected by external perturbations.

2.3. Pulsars in the Galactic Center

For a number of observational and theoretical considerations, we expect a large number of neutron stars in the central part of the Galaxy. For a comprehensive review of the observational evidence and related theoretical considerations, we refer to Wharton et al. (2012) and references therein. Based on evidence for, e.g., the past star formation rate, the expected initial stellar mass function in the Galactic Center environment, and the observations of massive stars and stellar remnants, overall up to

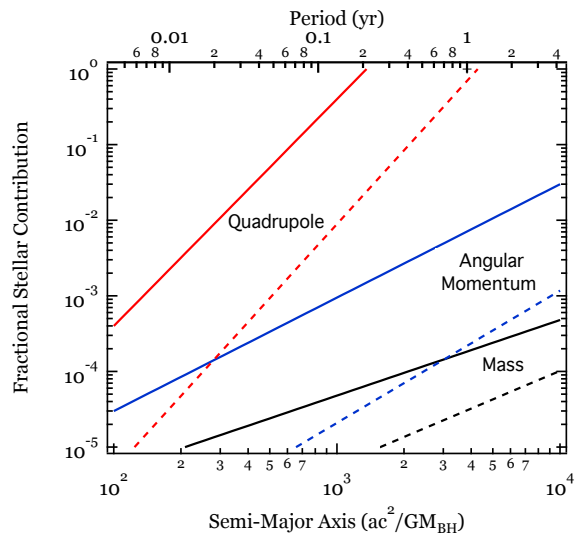


FIG. 1.— Fractional contribution to the black-hole mass, angular momentum, and quadrupole mass moment inside an orbit due to the enclosed distribution of objects. These fractional contributions represent the limiting accuracies to which the corresponding black-hole properties can be inferred using observations of orbits of stars and pulsars. The solid lines correspond to a stellar distribution with $\gamma = 2$, while the dashed lines correspond to $\gamma = 7/4$. The various other assumed parameters of the stellar cluster are given in equations (8), (10), and (13.)

100 normal pulsars and 1000 millisecond pulsars (MSPs) should be expected in the inner parsec. Earlier, Faucher-Giguère & Loeb (2011) pointed out that the high stellar density in the region allows also the effective creation of exotic binaries, like MSP-stellar black-hole binaries, which would be exciting laboratories in their own right (Wex & Kopeikin 1999; Liu et al. 2014).

Millisecond pulsars are old, recycled pulsars, which show typical periods between 1.4 and 30 ms, while normal pulsars have average periods of 0.5 to 1 s. millisecond pulsars also have spin-down rates and estimated magnetic field strengths that are typically three orders of magnitude smaller than those of normal (unrecycled) pulsars. These properties make millisecond pulsars superior – and hence preferred – clocks in pulsar timing experiments. For a normal pulsar, a typical timing precision is around $100 \mu\text{s}$, while for the best millisecond pulsars one can achieve a timing precision as good as 100 ns or better. In both cases, the final timing precision depends on the pulsar itself (e.g., the sharpness of its pulse shape, the intrinsic rotational stability) and the strength of the pulsar, as the error on an individual time-of-arrival (TOA) measurement scales with the signal-to-noise ratio of the observation (see Lorimer & Kramer 2004 for further details on pulsar properties and timing methods).

Despite concentrated efforts and dedicated searches in the Galactic Center region, the yield has been disappointingly low given the estimates. Until 2013, only five pulsars had been found within $15'$ of Sgr A*, with the closest of these $11'$ away, i.e., at a projected distance of about 25 pc (Johnston et al. 2006; Deneva et al. 2009; Bates et al. 2011). All of these were slow pulsars with dispersion measures up to 1500 pc cm^{-3} . Given their distances to Sgr A*, none of these are suitable for the experiments described below.

The resulting perceived paucity of Galactic Center pulsars had been explained as a consequence of hyper-strong scattering of the radio waves at the turbulent inhomogeneous interstellar plasma in the region. The scattering leads to temporal broadening of the pulses with expected timescales of at least $2000(\nu/1\text{ GHz})^{-4}\text{ s}$ (Cordes & Lazio 2002), rendering their detection impossible at typical search frequencies, around 1 to 2 GHz. For this reason, a number of high-frequency searches were conducted in the past (Kramer et al. 2000; Klein et al. 2004, Johnston et al. 2006; Deneva et al 2010; Macquart et al. 2010; Bates et al. 2011; Eatough et al. 2013; Siemion et al. 2013) at frequencies as high as 26 GHz. However, even in these searches, no pulsar in the central parsec was found. The currently best limit ($S_{min} < 10\ \mu\text{Jy}$ for a $S/N \sim 10$) is provided by observations with the 100-m Effelsberg telescope at 19 GHz (Eatough et al., in prep.).

The recent discovery of radio emission from the magnetar SGR J1745–29 by Eatough et al. (2013; see also Shannon & Johnston 2013), which had been first identified at X-rays (Kennea et al. 2013; Mori et al. 2013), provides an unexpected probe of the Galactic Center medium and the local pulsar population. The source that, with improved positional precision, is now named PSR J1745–2900, is located within $2.4''$ (or 0.1 pc projected) of Sgr A* (Bower et al. 2015) and is strong enough that even single pulses can be detected from a frequency of a few GHz (Spitler et al. 2014) up to an unprecedented 154 GHz (Torre et al. 2015). Below 1.1 GHz, the temporal broadening prevents a detection of the source (Spitler et al. 2014), while pulsed radio emission is detected up to 225 GHz, which is the highest frequency at which radio emission from a neutron star has been detected so far (Torre et al. 2015). The dispersion measure and the rotation measure of PSR J1745–2900 are the largest in the Galaxy (only the rotation measure of Sgr A* itself is larger; Eatough et al. 2013; Shannon & Johnston 2013), while the angular broadening of the source is consistent with that of Sgr A* (Bower et al. 2014, 2015), providing evidence for the proximity of the magnetar to the Galactic Center. While its rotational stability is unfortunately not sufficiently good to conduct precision timing experiments, it allows us to revisit the question of the hidden pulsar population.

Radio emitting magnetars are a very rare type of neutron stars and previously only three of them were known to exist in the Galaxy, i.e., less than 0.2% of all radio-loud neutron stars (Olausen & Kaspi 2014). The discovery of such a rare object adjacent to Sgr A* thereby supports the notion that many more ordinary radio pulsars should be present (Eatough et al. 2013; Chennamangalam & Lorimer 2014). A surprising aspect of the magnetar discovery is the relatively small scatter broadening that is observed (Spitler et al. 2014). With a pulse period of 3.75 s, its radio emission should not be detectable at frequencies as low as 1.1 GHz, if hyper-strong scattering were indeed present.

Imaging observations (Bower et al. 2015) resulted in the measurement of a proper motion that does not allow us yet to conclude as to whether the pulsar is bound to Sgr A*. It is possible that PSR J1745–2900 and the other five nearby pulsars originated from a stellar disk (see also Johnston et al. 2006) and that a central population of pulsars is still hidden. Indeed, Chennamangalam

& Lorimer (2014) argue that, even if the lower-than-expected scattering in the direction of PSR J1745–2900 is representative of the entire inner parsec, the potentially observable population of pulsars in the inner parsec has still a conservative upper limit of ~ 200 members. They conclude that it is premature to assume that the number of pulsars in this region is small.

In contrast, Dexter & O’Leary (2014) come to a different conclusion. They also revisited the question about the central pulsar population given the new constraints provided by the magnetar and the non-detection of previous high-frequency surveys. Considering various effects like depletion of the pulsar population due to kick velocities exceeding the central escape velocity, pulsar spectra and the apparent reduced scattering indicated by the magnetar observations (Spitler et al. 2014), they argue in favour of a “missing pulsar problem”. They also concluded that the magnetar discovery in the center may imply, in turn, an efficient birth process for magnetars in the central region. Similarly, others suggested that normal pulsars are not formed since they may collapse into black holes on comparably short timescales by accreting of dark matter (Bramante & Linden 2014).

At the core of deciding between these possibilities is our ability to properly model and account for all selection effects in the previous surveys. There are in fact indications that this is not the case. Firstly, continued monitoring of the scattering timescales for the magnetar indicates that the scattering time is highly variable. While it remains well below the prediction of hyper-strong scattering, it varies by a factor of 2 to 4 on timescales of months at frequencies between 1.4 and 8 GHz (Spitler et al., in prep.). This suggests that local “interstellar weather” certainly plays a role and that nearby scattering screens also affect the observed emission, making the resulting ability to observe sources overall line-of-sight dependent, especially at lower frequencies. This is not unexpected given the properties of the turbulent interstellar medium in the Galactic Centre. Rather than dealing with a uniform single screen, it is likely that we see the effects of multiple finite screens. In this case, secondly, one expects a much shallower frequency dependence of the scattering time than the canonical -4 values (Cordes & Lazio 2001). This is indeed seen for high-DM pulsars (Löhmer et al. 2001, 2004), where the scattering index is typically around ~ -3.5 for large dispersion measures. Spitler et al. (in prep.) find similar values for the magnetar. If this is indeed representative for a possible central pulsar or millisecond pulsar population, then the remaining scattering at 5, 14 or even 19 GHz would be underestimated in the analysis by Macquart et al. (2010) or Dexter & O’Leary (2014) by factors of 2.2, 3.7 or 4.3 respectively, when extrapolating from 1 GHz. Löhmer et al. (2001) measured even flatter frequency dependencies, which would make the discrepancy between real and estimated scattering times even larger. Unless more scatter broadening times in the Galactic centre are measured, this issue is difficult to settle. However, there is yet another, third effect that has been usually neglected in sensitivity calculations of pulsar surveys. As shown very recently by Lazarus et al. (2015) for the P-ALFA survey, red noise present in pulsar search data due to radio interference (RFI), receiver gain fluctuations, and opacity variations of the atmosphere cause a signifi-

cant decrease in sensitivity for pulsars with periods above 100 ms or so, when compared to the standard radiometer-based equation (see their Fig. 11). This would affect in particular a search for young pulsars, but also, of course, magnetars, which are nevertheless still easier to detect at high frequencies due to their much flatter flux density spectrum (Torre et al. 2015). This selection effect in particular would favour the detection of magnetars over that of normal, young pulsars and may explain in some respects the peculiarities of the current observational situation pointed out by Dexter & O’Leary. The work by Lazarus et al. demonstrates that the various selection effects are highly dependent on the individual surveys and that much more work is needed to understand the impact on the resulting search sensitivities.

Finally, none of the previous high-frequencies surveys has, to our knowledge, applied a fully coherent acceleration search. Such an acceleration search may be needed to account both for the movement of the pulsar around the central black hole, as well as for the presence of a binary companion. Indeed, due to the high stellar density, even exotic systems (e.g. MSP-stellar mass BH binary) may be expected (Faucher-Giguère & Loeb 2011). An acceleration search is usually very computationally expensive, especially for long integration times as employed in the high frequency searches (e.g. by Macquart et al. 2010 or Eatough et al., in prep.), since the parameter range to be searched scales as $\propto T_{obs}^3$. The lack of such an acceleration search contributes especially as a selection effect to the present non-detection of fast-spinning pulsars.

In order to model the selection effects (red noise, acceleration, scattering etc.) a more detailed study, taking also the orientation of the possible orbits and the change in acceleration into account, is needed. This is beyond the scope of this paper and will be presented elsewhere. It is clear, however, that selection effects are not adequately modelled so far and that more work is required.

We conclude that three scenarios are still possible: (a) The scattering seen for the Galactic Center magnetar is representative of the inner parsec. In this case, the pulsar population may be dominated by millisecond pulsars, for which this moderate scattering would still have prevented their detection at previous search frequencies. Higher frequency searches may therefore even allow the discovery and hence the exploitation of millisecond pulsars orbiting Sgr A* (see also Macquart & Kanekar 2015). We note in passing that the discovery of a millisecond pulsar population may settle an ongoing debate about a possible excess of GeV gamma ray photons from the Galactic Centre. It is being discussed whether such an excess could arise from the presence of dark matter or a central population of unresolved young or millisecond pulsars (see e.g. O’Leary et al. (2015) and references therein). Any pulsar discovery in the Galactic Centre would make a dark matter discovery less likely. (b) There is a reduced number of pulsars in the Galactic Center region that is consistent with selection effects. For example, the lack of dispersion makes the discovery of unknown pulsars actually more difficult at high frequencies as the signals are more difficult to be distinguished from radio interference (see Eatough et al., in prep.), or (c) PSR J1745–2900 is indeed in front of a much more

severe scattering screen but the scattering properties for particular line-of-sights are changing with time due to “local weather” effects, signs of which have been already detected (Spitler et al., in prep.). In this case, search observations at even higher frequencies are required and still promising.

Given that we cannot distinguish between these scenarios based on the available data, high frequencies searches will continue. The use of more sensitive instruments than available in the past, e.g., ALMA or the Square Kilometre Array (SKA), may therefore lead to the discovery of normal pulsars and even millisecond pulsars. In considering how they can be used to measure the properties of Sgr A*, we will therefore assume a variety of obtainable timing precisions. For details, we refer the reader to Liu et al. (2012), who demonstrated possible precision levels as a function of observing frequency for the SKA and 100-m class telescopes. In their arguments, Liu et al. (2012) only considered normal pulsars and also assumed a hyper-strong scattering. If the latter is not present as we have discussed above, millisecond pulsars may be detectable (although this may require proper acceleration searching). Hence, for the discussion of the measurable effects, we will also allow for this possibility that a millisecond pulsars will be detected.

There are a number of millisecond pulsars in globular clusters at distances that are significantly larger than that of the Galactic centre. It is not uncommon to achieve a timing precision of about $10 \mu\text{s}$ for these distant sources. The exact precision depends foremostly on the strength of the pulsar signal and the sensitivity of the telescope, as well as the sharpness of some of the detectable profile features. If we need to go to high radio frequencies in order to beat interstellar scattering to see pulsars in the center of the Milky Way, the flux density decreases and timing precision decreases accordingly. This can be compensated by larger bandwidth or bigger telescopes. As shown in Eatough et al. (2015), a timing precision of $1 \mu\text{s}$ should be routinely possible with the SKA, even at distances of the Galactic centre at higher frequencies. Such a precision is certainly more challenging with existing instruments. Overall, in order to cover all three plausible scenarios discussed above, we will assume, in the following, that a Galactic Center pulsar can be timed with a precision of 1, 10, and $100 \mu\text{s}$. As, in principle, only one pulsar is needed to extract the black-hole parameters, we consider this to be a useful range to demonstrate the effects that we can expect to measure.

2.4. Relativistic Orbital Effects

In describing the orbit of a stellar-mass object around Sgr A*, we will use the coordinate system and notation shown in Figure 2. In particular, we will denote by m_* the mass of the orbiting object and by a and e the semi-major axis and eccentricity of its orbit. We will use the vector \mathbf{S}_\bullet to define the black-hole spin and the vector \mathbf{K}_0 to denote the line-of-sight unit vector pointing from the Earth to the black hole. We will also denote the longitude of the periapsis of the orbit with respect to the equatorial plane of the black hole by ω , the location of the ascending node by Υ , and the inclination of the orbit with respect to the black-hole spin axis by Θ .

With these definitions, the Newtonian period of the

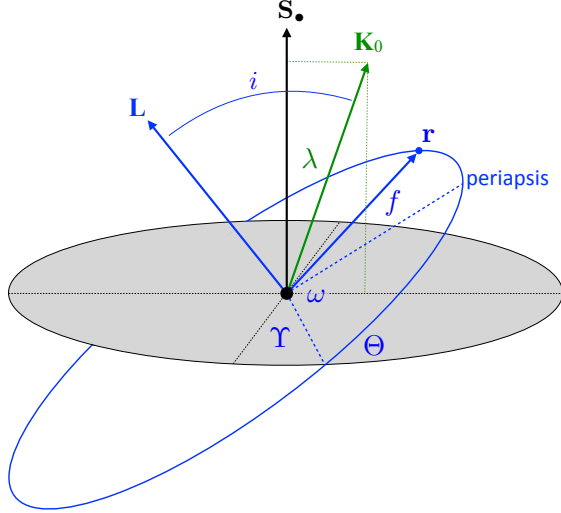


FIG. 2.— Coordinate system and notation used in defining an orbit of a stellar-mass object around Sgr A*. The vector \mathbf{S}_\bullet denotes the spin of Sgr A* and \mathbf{K}_0 is line-of-sight unit vector pointing from the Earth to the black hole. The longitude of the periastris of the orbit is ω , the location of the ascending node is Υ , and the inclination of the orbit with respect to the black-hole spin axis is Θ . The angle i , between \mathbf{K}_0 and the orbital angular momentum \mathbf{L} , is the inclination of the orbit with respect to the observer.

orbit is

$$P = 2\pi \left(\frac{a^3}{GM_\bullet} \right)^{1/2} = 133.1 \left(\frac{M_\bullet}{4 \times 10^6 M_\odot} \right) \left(\frac{ac^2}{GM_\bullet} \right)^{3/2} \text{ s}. \quad (14)$$

Eccentric orbits of stars and pulsars precess on the orbital plane (relativistic periastris precession). The leading term comes from the mass-monopole M_\bullet and corresponds to the relativistic precession of the Mercury orbit (Einstein 1915). The advance of periastris per orbit is $\Delta\omega = 2\pi k$, where

$$k = \frac{3}{1-e^2} \left(\frac{2\pi GM_\bullet}{Pc^3} \right)^{2/3} = \frac{3}{1-e^2} \left(\frac{GM_\bullet}{c^2 a} \right). \quad (15)$$

This corresponds to a characteristic timescale for this precession of (see Merritt et al. 2010 for the definition, who denote this by t_S)

$$t_M \equiv \frac{\pi P}{\Delta\omega} = \frac{P}{6} \frac{c^2 a}{GM_\bullet} (1-e^2) = 22.18 \left(\frac{M_\bullet}{4 \times 10^6 M_\odot} \right) \left(\frac{ac^2}{GM_\bullet} \right)^{5/2} (1-e^2) \text{ s} \quad (16)$$

In this expression, we have neglected the small contributions of the spin and of the quadrupole of the black hole.

Orbits with angular momenta that are not parallel to the spin \mathbf{S}_\bullet of the black hole show a precession of the orbital angular momentum around the \mathbf{S}_\bullet direction due to frame dragging (Lense-Thirring precession of the nodes). The location of the ascending node of the orbit, Υ , advances per orbit by

$$\Delta\Upsilon = \Omega_{\text{LT}} P \quad (17)$$

where

$$\Omega_{\text{LT}} \equiv \frac{8\pi^2}{(1-e^2)^{3/2}} \frac{GM_\bullet}{c^3 P^2} \chi \quad (18)$$

is the Lense-Thirring frequency. The characteristic timescale for this process is (Merritt et al. 2010)

$$t_J \equiv \frac{\pi P}{\Delta\Upsilon} = \frac{P}{4\chi} \left[\frac{c^2 a (1-e^2)}{GM_\bullet} \right]^{3/2} = 33.27 \chi^{-1} \left(\frac{M_\bullet}{4 \times 10^6 M_\odot} \right) \left(\frac{ac^2}{GM_\bullet} \right)^3 (1-e^2)^{3/2} \text{ s}. \quad (19)$$

Finally, tilted orbits also precess because of the quadrupole moment of the spacetime with a characteristic timescale (Merritt et al. 2010)

$$t_Q = \frac{P}{3|q|} \left[\frac{c^2 a (1-e^2)}{GM_\bullet} \right]^2 = 44.35 |q|^{-1} \left(\frac{M_\bullet}{4 \times 10^6 M_\odot} \right) \left(\frac{ac^2}{GM_\bullet} \right)^{7/2} (1-e^2)^2 \text{ s}. \quad (20)$$

Figure 3 shows the characteristic timescales of these relativistic orbital effects as a function of the semi-major axes and orbital periods of the orbits. A number of additional relativistic effects related to time dilation and photon propagation (Shapiro delay) can also be detected during timing observations of pulsars. We will discuss these effects and their dependence on the pulsar orbital parameters in §4.

2.5. Optimal Orbital Parameters for Stars and Pulsars

Performing tests of the no-hair theorem with orbits is hampered by a number of astrophysical complexities caused by non-relativistic phenomena that affect, in principle, the orbits. These included the self-interaction between the stars in the stellar cluster (Merritt et al. 2010; Sadeghian & Will 2011), the hydrodynamic drag between the stars and the accretion flow (Psaltis 2012), as well as stellar winds and tidal deformations (Psaltis, Li, & Loeb 2012). In order to identify the orbital parameters of stars that are optimal for performing the test of the no-hair theorem, we will first summarize and combine the results of these studies.

Interactions with Other Stars.—Merritt et al. (2010) and Sadeghian & Will (2011) explored the decoherence of the orbit of a star (or pulsar) due to Newtonian gravitational interactions within the inner stellar cluster. They obtained an approximate expression for the decoherence timescale given by

$$t_N = \frac{P}{q_* \sqrt{N(a)}}, \quad (21)$$

where $q_* \equiv m_*/M_\bullet$ is the average ratio of the mass of a star (or compact object) in the cluster to that of Sgr A*, and $N(a)$ is the number of stars inside the orbit of the object under consideration.

Using equations (6), (14), and (21), we obtain for the decoherence timescale of orbits due to the self interaction

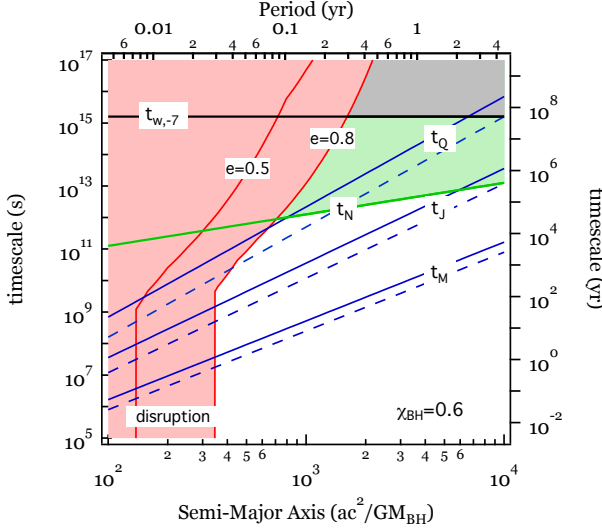


FIG. 3.— Characteristic timescales for various relativistic and astrophysical effects that alter the orbits of stars around Sgr A*. The three blue lines correspond to the periastris precession (t_M), and orbital plane precession due to frame dragging (t_J) and due to the quadrupole of the black hole (t_Q), for orbits with eccentricities of $e = 0.5$ (solid) and $e = 0.8$ (dashed), respectively; the spin of Sgr A* is set to $\chi = 0.6$. The green line corresponds to the orbital decoherence timescale (t_N) due to the interactions with other objects in the stellar cluster. The black curve ($t_{w,-7}$) corresponds to the orbital evolution timescale due to the launching of a stellar wind. The red curves correspond to the orbital evolution due to the tidal dissipation of orbital angular momentum for two eccentricities. Stars in orbits with semi-major axes comparable to 1000 gravitational radii are optimal targets for observing post-Schwarzschild relativistic effects.

between objects in the stellar cluster

$$\begin{aligned}
 t_N &= 2\pi \left(\frac{M_\bullet}{M_* m_*} \right)^{1/2} \left(\frac{a}{a_0} \right)^{-1/2} \left(\frac{a^3}{GM_\bullet} \right)^{1/2} \\
 &= 12.6 \times 10^8 \left(\frac{M_\bullet}{4.3 \times 10^6 M_\odot} \right)^{3/2} \left(\frac{M_*}{10^6 M_\odot} \right)^{-1/2} \\
 &\quad \left(\frac{m_*}{M_\odot} \right)^{-1/2} \left(\frac{a_0}{1 \text{ pc}} \right)^{-1/2} \left(\frac{ac^2}{GM_\bullet} \right) \text{ s}. \quad (22)
 \end{aligned}$$

Figure 3 compares the Newtonian decoherence timescale with those of the three relativistic effects discussed in §2. For the parameters of Sgr A* and of the stellar cluster around it, stars with orbital periods less than ~ 1 yr are required in order for the Newtonian interactions not to mask the orbital plane precession due to frame dragging (see a more detailed discussion and simulations in Merritt et al. 2010).

Hydrodynamic Interactions with the Accretion Flow.— In Psaltis (2012), we investigated the changes in the orbits of stars and pulsars caused by the hydrodynamic and gravitational interactions between them and the accretion flow around Sgr A*. For all cases of interest, we found that the hydrodynamic drag is the dominant effect. However, as we will show below, even the hydrodynamic drag is negligible for the orbital separations considered here.

When a star of mass m_* and radius R_* plows through the accretion flow of density ρ with a relative velocity

u_{rel} , it feels an effective acceleration equal to

$$a_d = \frac{\pi R_*^2 \rho u_{\text{rel}}^2}{m_*}. \quad (23)$$

We can use this acceleration to define a characteristic timescale for the change of the orbital parameters as

$$t_d \equiv \frac{u_{\text{rel}}}{a_d} = \frac{m_*}{\pi R_*^2 \rho u_{\text{rel}}}. \quad (24)$$

Setting the relative velocity equal to the orbital velocity of a circular orbit, and the density of the accretion flow to

$$\rho = m_p n_e^0 \left(\frac{ac^2}{GM_\bullet} \right)^{-1.1} \quad (25)$$

which has been inferred observationally (see discussion in Psaltis 2012), we obtain

$$\begin{aligned}
 t_d &= \frac{m_*}{\pi R_*^2 m_p n_e^0 c} \left(\frac{ac^2}{GM_\bullet} \right)^{1.6} \\
 &= 7.5 \times 10^{15} \left(\frac{m_*}{10 M_\odot} \right) \left(\frac{R_*}{10 R_\odot} \right)^{-2} \\
 &\quad \left(\frac{n_e^0}{3.5 \times 10^7 \text{ cm}^{-3}} \right)^{-1} \left(\frac{ac^2}{GM_\bullet} \right)^{1.6} \text{ s}. \quad (26)
 \end{aligned}$$

Here, m_p is the mass of the proton and we assumed for simplicity that the orbit is circular. This timescale is significantly larger than all other timescales shown in Figure 3.

Stellar Winds.— In Psaltis et al. (2012), we explored the change in the orbital parameters of a stars due to the launching of a wind that carries a fraction of the orbital energy and angular momentum. The semi-major axis and the eccentricity of the orbit change at a timescale comparable to $t_w \equiv m_*/\dot{M}_w$, where \dot{M}_w is the rate of wind mass loss, i.e.,

$$t_{w,-7} = 3.2 \times 10^{15} \left(\frac{m_*}{10 M_\odot} \right) \left(\frac{|\dot{M}_w|}{10^{-7} M_\odot \text{ yr}^{-1}} \right)^{-1} \text{ s}, \quad (27)$$

where we have used the subscript “-7” to denote the exponent in the wind mass loss rate. As shown in Figure 3, the evolution of the stellar orbit due to the launching of a stellar wind is always negligible compared to the effects of the Newtonian interactions with the other stars in the cluster.

Tidal Evolution.— Finally, in Psaltis et al. (2012), we also explored the evolution of a stellar orbit due to the tidal dissipation of orbital energy during the periastris passages. Even though tidal dissipation does not cause a significant precession in the orbit (see Sadeghian & Will 2011), it leads to an evolution of the semi-major axis that may be misinterpreted (due to the expected low signal-to-noise ratio in the observations) as a change in the projected orbital separation caused by orbital precession.

The characteristic timescale for orbital evolution due to tidal dissipation is

$$t_d \equiv \frac{E}{\Delta E / \Delta t}$$

$$\begin{aligned}
 &= \frac{\pi R_*}{c} \left(\frac{GM_\bullet}{c^2 R_*} \right)^6 \left(\frac{m_*}{M_\bullet} \right) \left(\frac{ac^2}{GM_\bullet} \right)^{13/2} (1-e)^6 T_2^{-1} \\
 &= 0.98 \times 10^{-4} \left(\frac{M_\bullet}{4.3 \times 10^6 M_\odot} \right)^5 \left(\frac{R_*}{10 R_\odot} \right)^{-5} \\
 &\quad \left(\frac{m_*}{10 M_\odot} \right) \left(\frac{ac^2}{GM_\bullet} \right)^{13/2} (1-e)^6 T_2^{-1}(\eta) \text{ s}, \quad (28)
 \end{aligned}$$

where the quantity $T_2(\eta)$ is defined and calculated in Psaltis et al. (2012). Also, if the star at periastron reaches inside the tidal radius

$$R_t = R_* \left(\frac{M_\bullet}{m_*} \right)^{1/3}, \quad (29)$$

it gets disrupted. Both these effects, for two different orbital eccentricities, are shown in Figure 3.

Optimal parameters.— Comparing the various constraints shown in Figure 3 to the characteristic timescales of the three relativistic effects allows us to identify the optimal orbital parameters of stars and pulsars for measuring the black-hole spin and for testing the no-hair theorem.

Using the orbital precession of stellar orbits to measure the spin of Sgr A* simply requires sub-year orbital periods, for the effects of the stellar perturbations to become negligible (as previously discussed in Merritt et al. 2010). On the other hand, measuring the black-hole quadrupole requires stars in much tighter orbits ($\lesssim 0.1$ yr), for the stellar perturbations to be negligible, but with moderate eccentricities ($e \lesssim 0.8$), for tidal effects to not interfere with the measurements of the relativistic precessions (see also Will 2008).

For the case of pulsar timing, tidal effects do not alter the orbits and, therefore, only stellar perturbations can limit our ability to observe relativistic precessions. If we were to use pulsar timing to measure the black-hole quadrupole by observing the pulsar orbital plane precession, we would still be limited to using only rather tight orbits ($\lesssim 0.1$ yr). However, in defining the characteristic timescale for quadrupole effects on the pulsar orbits (eq. [20]), we have only considered the secular precession of the orbit. The most promising way to extract the quadrupole moment from timing observations is through the periodic effects in the orbital motion of the pulsar caused by the quadrupolar structure of the gravitational field of Sgr A* (Wex & Kopeikin 1999; Liu et al. 2012). This is not only the case for the quadrupole but also for the relativistic precession of the periastron due to the mass monopole (Damour & Deruelle 1985) and the precession of the orbit due to the frame dragging (Wex 1995). (See also the discussion in Angéilil & Saha 2014.) As argued by Liu et al. (2012), such unique periodic features in the timing of a pulsar around Sgr A* provide a powerful handle to correct for external perturbations. As we will demonstrate with mock data simulations in §4, timing a pulsar only during a small number of successive periastron passages is sufficient to measure both the spin and the quadrupole moment of Sgr A*.

3. PROBING THE SPACETIME OF Sgr A* WITH STARS

Astrometric and spectroscopic studies of stars in the near vicinity of the black-hole horizon will allow detecting a number of relativistic effects that depend on the

spin and the quadrupole moment of the black hole. Two of these effects will be the dominant ones (see discussion in Angéilil et al. 2010). The first is the precession of the periastron of an elliptical orbit on the orbital plane, which will lead primarily to a very accurate measurement of the black-hole mass (see, e.g., Weinberg et al. 2005). The second is the precession of the orbital plane due to frame dragging, which depends on both the spin and the quadrupole moment of the black hole. Measuring the latter for two or more stars, will allow disentangling their effects on the orbits and hence lead, in principle, to a test of the no-hair theorem (Will 2008).

In the context of a stellar orbit around Sgr A*, we write the secular rate of change of the location of its periastron as (Merritt et al. 2010)²

$$\dot{\omega} = \frac{\pi}{t_M} - \frac{3\pi}{t_J} \cos \Theta - \frac{\pi}{2t_Q} (1 - 5 \cos^2 \Theta) \quad (30)$$

and the rate of precession of its orbital plane as

$$\dot{\Upsilon} = \frac{\pi}{t_J} - \frac{\pi}{t_Q} \cos \Theta, \quad (31)$$

where the various characteristic timescales were defined in §2. A change in either of these angles will correspond to an angular displacement in the sky that will need to be measured astrometrically. Because of the large lever arm of an eccentric orbit, the accuracy of such a measurement will be determined by the ability of the observations to detect changes in the position of the sky during apoapsis passages. In other words, the two relevant quantities are the total angular displacement of the apparent position of the apoapsis after N orbits, i.e.,

$$\begin{aligned}
 \Delta\theta_{\text{apoapsis}} &= NP\dot{\omega} \frac{a(1+e)}{D} \cos i \\
 &= N \frac{1+e}{1-e^2} \left(\frac{GM_\bullet/c^2 D}{5.12 \mu\text{as}} \right) \cos i \mu\text{as} \left[96.8 \right. \\
 &\quad \left. - 192.8\chi \left(\frac{ac^2}{GM_\bullet} \right)^{-1/2} (1-e^2)^{-1/2} \cos \Theta \right. \\
 &\quad \left. - 4.7|q| \left(\frac{ac^2}{GM_\bullet} \right)^{-1} (1-e^2)^{-1} (1-5\cos^2 \Theta) \right] \quad (32)
 \end{aligned}$$

and the total angular displacement in the apparent position of the line of nodes, i.e.,

$$\begin{aligned}
 \Delta\theta_{\text{node}} &= NP\dot{\Upsilon} \frac{a(1+e)}{D} \cos i \\
 &= N \frac{1+e}{(1-e^2)^{3/2}} \left(\frac{ac^2}{GM_\bullet} \right)^{-1/2} \left(\frac{GM_\bullet/c^2 D}{5.12 \mu\text{as}} \right) \cos i \mu\text{as} \\
 &\quad \left[12.6\chi - 9.4|q| \left(\frac{ac^2}{GM_\bullet} \right)^{-1/2} (1-e^2)^{-1/2} \cos \Theta \right]. \quad (33)
 \end{aligned}$$

For a star at an orbital separation of $1000 GM_\bullet/c^2$ with an eccentricity of $e = 0.8$ around a Kerr black hole that is maximally spinning, tracing the orbit over 5 years

² Note, Merritt et al. (2010) use $\varpi \equiv \omega + \Upsilon \cos \Theta$.

($N \simeq 38$) will lead to a total angular displacement of the apparent position of the periastron of $\Delta\theta_{\text{apoapsis}} \simeq 8$ mas and of the apparent position of the line of nodes of $\Delta\theta_{\text{node}} \simeq 300 \mu\text{as}$. Observations with a future 30-m class telescope are expected to have an accuracy of $\sim 500 \mu\text{as}$ (Weinberg et al. 2005), while simulations of tracing of stellar orbits with GRAVITY suggest an accuracy of $\sim 10 - 200 \mu\text{as}$, depending on the brightness of the star (Stone et al. 2012). Since our goal is to use stellar observations to measure the precession of their orbital planes, we will focus on future observations with GRAVITY and assume nominal uncertainties in the relative astrometric positions of $\sigma_\theta = 10 \mu\text{as}$ and $\sigma_\theta = 100 \mu\text{as}$.

The uncertainties in the measurement of the black-hole properties will be determined primarily by the ability of the experiment to measure the advance of the apoapsis between orbits. If we approximate the procedure as consisting of measuring the differential astrometric location of the apoapsis once per orbital period with an uncertainty σ_θ , then the uncertainty in the inferred rate of (apoapsis or orbital-plane) precession after N measurements (i.e., orbits) that are equidistant in time will be (see Press et al. 1992)

$$\sigma_{\text{rate}}^2 = \frac{S}{S S_{tt} - S_t^2}, \quad (34)$$

where

$$\begin{aligned} S &\equiv \frac{N}{\sigma_\theta^2} \\ S_t &\equiv \sum_{i=1}^N \frac{(i-1)P}{\sigma_\theta^2} = \frac{N(N-1)}{2\sigma_\theta^2} P \\ S_{tt} &\equiv \sum_{i=1}^N \frac{(i-1)^2 P^2}{\sigma_\theta^2} = \frac{N(2N^2 - 3N + 1)}{6\sigma_\theta^2} P^2. \end{aligned} \quad (35)$$

For $N \gg 1$, the uncertainty in the total displacement after N orbits is

$$\sigma_{\Delta\theta} = NP\sigma_{\text{rate}} = \left(\frac{12}{N}\right)^{1/2} \sigma_\theta \quad (36)$$

and the uncertainty in the inferred rate of precession is

$$\sigma_{\text{rate}} = \left(\frac{12}{N}\right)^{1/2} \frac{\sigma_\theta}{NP}. \quad (37)$$

In order to illustrate the prospect of measuring the black-hole properties using such measurements, we will assume that GRAVITY is able to trace for $N = 40$ orbits the trajectories of two stars with orbital separations of 800 and $1000 GM_\bullet/c^2$, with orbital eccentricities of 0.9 and 0.8, respectively, and with the cosines of all relevant orientations set to 0.5. We chose these orbits such that the dynamical precession is faster than the other complicating astrophysical effects we considered in §2.4 (see Figure 2) and the enclosed mass, angular momentum, and quadrupole moment of the stellar cluster will not affect the measurements significantly.

Our goal is to estimate the posterior likelihood that a given black-hole spin and quadrupole moment are con-

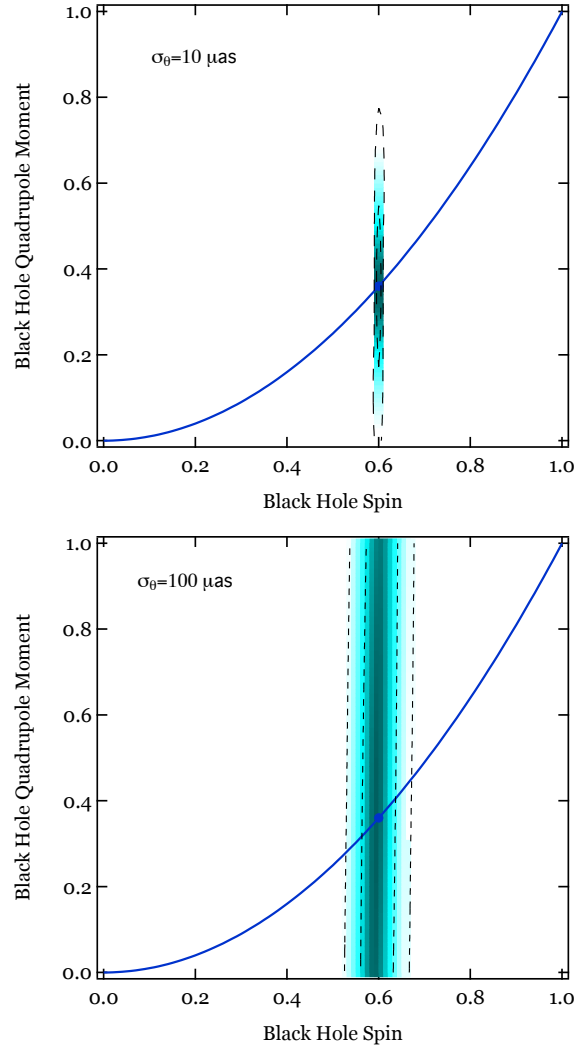


FIG. 4.— The posterior likelihood of measuring the spin and quadrupole moment of Sgr A* by tracing the orbits of two stars with GRAVITY, assuming an astrometric precision of (top) $10 \mu\text{as}$ and (bottom) $100 \mu\text{as}$. The dashed curves show the 68% and 95% confidence limits, while the solid curve shows the expected relation between these two quantities in the Kerr metric. The filled circle marks the assumed spin and quadrupole moment ($\chi = 0.6$, $|q| = 0.36$). The two stars are assumed to have orbital separations equal to 800 and $1000 GM_\bullet/c^2$ and eccentricities of 0.9 and 0.8, respectively. Even at these relatively small orbital separations, tracing the orbits of stars primarily measures the spin of the black hole, unless a very high level of astrometric precision is achieved.

sistent with the set of measurements, i.e.,

$$P(\chi, q|\text{data}) = P(\text{data}|\chi, q)P(\chi)P(q). \quad (38)$$

Here $P(\chi)$ and $P(q)$ are the priors on the black-hole spin and quadrupole moment, which we take to be constant between zero and unity. We also assume that the astrometric measurements for the two stars are independent of each other (which will almost certainly not be true in reality), such that

$$P(\text{data}|\chi, q) = \prod_{i=1}^2 P_{\text{apo}}(i, \text{data}|\chi, q)P_{\text{node}}(i, \text{data}|\chi, q) \quad (39)$$

and $P_{\text{apo}}(i, \text{data}|\chi, q)$ and $P_{\text{node}}(i, \text{data}|\chi, q)$ are the

posterior likelihoods that a given black-hole spin and quadrupole moment will generate the measurements for the apoapsis and nodal precession of the i -th star, respectively. We assume that the last two likelihoods for each star are Gaussian, with centroids equal to the fiducial values that correspond to the orbits of the stars around a Kerr black hole of spin $\chi = 0.6$, and with dispersions $\sigma_{\Delta\theta}$ given by equation (36) with $\sigma_\theta = 10 \mu\text{as}$ and $\sigma_\theta = 100 \mu\text{as}$.

Figure 4 shows the resulting posterior likelihood over the black-hole mass and quadrupole moment, for the simulation parameters discussed above. As expected, even though using two stars would allow us, in principle, to break the degeneracy between the spin and the quadrupole moment of the black hole, in practice, GRAVITY observations will be able to predominantly measure the spin of the black hole. This, of course, can be performed even with following the orbit of a single star. In that case, using equation (33), we can estimate the accuracy to which GRAVITY observations will lead to a measurement of the black-hole spin as

$$\sigma_\chi \sim 0.064 \left(\frac{\sigma_\theta}{100 \mu\text{as}} \right) \left(\frac{N}{40} \right)^{-3/2} \left(\frac{ac^2/GM_\bullet}{1000} \right)^{1/2} \left(\frac{GM_\bullet/c^2 D}{5.1 \mu\text{as}} \right)^{-1} \left[\frac{(1-e)(1-e^2)^{1/2}}{0.12} \right] \left(\frac{\cos i}{0.5} \right)^{-1}. \quad (40)$$

In this last expression, we have neglected the correlated uncertainties between the measurement of the spin of the black hole and of the orientation of the orbit with respect to the spin. Nevertheless, our estimates here show the ability of astrometric tracing of stellar orbits with GRAVITY to determine the spin of Sgr A* and to provide an independent probe that will allow us to control and quantify possible systematic effects in the measurement.

4. PROBING THE SPACETIME OF Sgr A* WITH A PULSAR

As demonstrated by Wex & Kopeikin (1999) and Liu et al. (2012), a single pulsar orbiting Sgr A* at similar distances as discussed for stellar orbits earlier will allow us to extract the relevant black-hole parameters with high precision, even if only a moderate timing precision can be achieved. In order to gauge the feasibility of such an experiment, we are, of course, limited by two major uncertainties. One is the existence of detectable and timeable pulsars in appropriate distances to the central black hole, and the other is the impact of potential perturbations to the pulsar orbits due to external effects.

We addressed the first source of uncertainty in §2.3. In order to address the second, we expand here on the earlier work by Wex & Kopeikin (1999) and Liu et al. (2012), who presented the fundamental recipe of this experiment. The work presented here goes further, providing a major step towards the development of a timing formula that can be used to exploit the pulsars once they are discovered. In particular, it makes use of a timing model that consistently includes the periodic spin contributions derived in Wex (1995), where the orbital motion in the reference frame of the black hole (Fig. 2) is described by the following quasi-Keplerian parametrization

$$n(t - t_0) = u - e_t \sin u, \quad (41)$$

$$f = 2 \arctan \left[\left(\frac{1 + e_\varphi}{1 - e_\varphi} \right)^{1/2} \tan \frac{u}{2} \right], \quad (42)$$

$$r = a(1 - e_r \cos u), \quad (43)$$

$$\varphi = \omega_0 + (1 + k)f, \quad (44)$$

$$\Upsilon = \Upsilon_0 + w(f + e \sin f). \quad (45)$$

The orbital frequency n is related to the orbital period P via $n = 2\pi/P$. The angle ω_0 gives the location of the periapsis at $t = t_0$. The three eccentricities e_t , e_φ and e_r are different from each other only at the first post-Newtonian (pN) level, and the quantities k and w are of 1pN and 1.5pN order, respectively.

A comment on the practical use of above equations: The parametrization of the orbital motion in equations (41)–(45) represents a simple extension of the elegant quasi-Keplerian solution of the 1pN two-body problem, found by Damour & Deruelle (1985). The latter is the basis of the DD timing model (Damour & Deruelle 1986), which is implemented in TEMPO, the standard software for pulsar timing³. For this reason, we could easily extend TEMPO to include spin-orbit and, as we discuss later, quadrupole effects. This modified TEMPO version forms the basis of our mock data simulations.

The location of the periapsis at a time t is given by

$$\omega = \omega_0 + kf. \quad (46)$$

Consequently the advance of periapsis is linear in the true anomaly, and, therefore, non-linear in time. For highly eccentric orbits, the advance of the periapsis is clearly faster when the pulsar is near the central black hole. The orbital averaged precession rate is given by

$$\langle \dot{\omega} \rangle = kn. \quad (47)$$

As evident from equation (45), a similar behavior comes with the periodic spin contributions, where the orbital averaged precession of the nodes (Lense-Thirring precession) is given by

$$\langle \dot{\Upsilon} \rangle = wn. \quad (48)$$

Both, k and w are free parameters of the timing model. For a given theory of gravity, they depend on the Keplerian parameters of the pulsar orbit and on the mass and the spin of the central black hole.

At this point it is important to note that ω is not the longitude of periapsis that enters the pulsar-timing model directly. The timing model makes use of the longitude of periapsis with respect to the plane of the sky, and we denote it by $\tilde{\omega}$. Its relation to ω depends on the orientation of the black-hole spin with respect to the observer and can be found in Wex & Kopeikin (1999).

In the following, we first discuss the various relativistic effects that allow us to use pulsar timing in order to measure the mass, the spin, and the quadrupole moment of the central black hole. Then, using the new timing model, we show in mock data simulations that it is sufficient to time the pulsar when it moves near Sgr A* in order to determine the mass, spin, and quadrupole moment of the black hole. As a consequence, the no-hair theorem test with a pulsar turns out to be fairly robust

³ There are two TEMPO versions in use, TEMPO (<http://tempo.sourceforge.net/>) and TEMPO2 (Hobbs et al. 2006). For our simulations we used a modified version of TEMPO.

against external perturbations. Furthermore, we investigate the possibility to fully determine the spatial orientation of the Sgr A* spin and give an estimate for a distance measurement from timing.

4.1. Mass Determination

It is well known that the measurement of post-Keplerian (PK) parameters in binary pulsars can provide highly accurate measurements of the masses of the system (Lorimer & Kramer 2004). The same can be expected for a pulsar in orbit around Sgr A*, where the situation is insofar different as the pulsar is like a test particle, whose mass is negligible in comparison to the companion's mass, i.e., the 4.3 million solar masses of Sgr A*. In such a situation the measurement of a single PK parameter allows the determination of the mass of Sgr A*, once a theory of gravity is assumed. The measurement of a second PK parameter already allows for a consistency check, since the inferred mass should agree with the one from the first PK parameter (Liu et al. 2012).

In the following, we quickly summarize the most important relativistic effects and their leading order expression within GR (see Lorimer & Kramer 2004, and references therein for details).

- The advance of periastron per orbit is $\Delta\omega = 2\pi k$, where k was defined in equation (15). For a fast spinning black hole, k can have a significant contribution from frame-dragging effects, as we will discuss in more detail below.
- The time dilation (Einstein delay) has an amplitude of

$$\gamma_E = 2\frac{e}{n} \left(\frac{GM_\bullet}{c^3 n} \right)^{2/3}. \quad (49)$$

- The signal propagation delay (Shapiro delay), which is proportional to the black hole mass, reads as a function of the true anomaly f as

$$\Delta_S = \frac{2GM_\bullet}{c^3} \ln \left[\frac{1 + e \cos f}{1 - \sin i \sin(\tilde{\omega} + f)} \right]. \quad (50)$$

A measurement of the Shapiro delay, simultaneously gives M_\bullet and $\sin i$ (see Figure 2 for the definition of the inclination angle i). The latter is connected to M_\bullet via the so-called mass function

$$\sin i = nx \left(\frac{GM_\bullet}{c^3 n} \right)^{-1/3}. \quad (51)$$

The Keplerian parameter $x \equiv a \sin i / c$ is the projected semi-major axis of the pulsar orbit and can be measured with high precision from pulsar timing. Consequently, there are two ways to extract the mass of Sgr A* from a measurement of the Shapiro delay.

Based on a consistent covariance analysis using mock data simulations, Liu et al. (2012) demonstrated that a pulsar in a close orbit ($P_b \sim 1$ yr) around Sgr A* allows for a very precise determination of its mass, M_\bullet . Even a moderate timing precision can lead to a $\sim 10^{-5}$ precision for M_\bullet , since there are various relativistic effects that can be utilized for mass determination. The simulations in

Liu et al. (2012), however, were based on the assumption that the pulsar can be timed continuously over several years, covering at least a few full orbits. Later in this section, we relax this assumption and allow for a situation where, due to external perturbation, only the timing data near the black hole can be used in a phase-connected solution. As it turns out, in particular the Einstein and the Shapiro delay provide a robust determination of M_\bullet that is only weakly affected by external perturbations or uncertainties in our knowledge of the spin of Sgr A*.

4.2. Frame Dragging and Spin Measurement

The dragging of inertial frames by the rotation of the black hole affects the precession of the periastron of the orbit. Indeed, beyond leading order, equation (15) would include a Lense-Thirring contribution k_{LT} , where

$$k_{LT} = -3 \frac{\Omega_{LT}}{n} \cos \Theta \quad (52)$$

(see also equation [30]). An independent measurement of the mass M_\bullet , for instance through the Shapiro delay, could then be used to compute $\chi \cos \Theta$, within GR, where $\chi \cos \Theta \leq 1$ is required by the cosmic censorship conjecture.

The most prominent effect of frame dragging in the pulsar motion is the Lense-Thirring precession of the orbital plane. In GR, the nodes of the orbit precess at an averaged rate of

$$\langle \dot{\Upsilon} \rangle = wn = \Omega_{LT}, \quad (53)$$

(see also equation [31]). Although w is a small quantity ($\sim 10^{-4} \chi$ for a 0.1 yr orbit), given the large size of a pulsar orbit around Sgr A*, it has a tremendous impact on the timing residuals. In fact, for orbits $\lesssim 1$ yr, it leads to a large change in the projected semi-major axis, x , giving rise to a significant time evolution of x , that can be measured as a first derivative \dot{x} and even a second derivative \ddot{x} . Furthermore, it also leads to an observable second derivative in the advance of the periastron, $\ddot{\omega}$ (see Liu et al. 2012 for details).

As can be seen from equation (45), the location of the ascending node, Υ , advances non-linearly in f and t , which we will exploit for the first time in this paper. Instead of using only the secular contributions \dot{x} , \ddot{x} , and $\ddot{\omega}$ to model the changes in the orbit due to Lense-Thirring precession, we implement the full model equations (41)–(45), therefore also accounting for the periodic contributions. The latter is of particular importance, if the pulsar is in a highly eccentric orbit. Moreover, this will turn out to be extremely valuable in the presence of external perturbations. In fact, Liu et al. (2012) have already argued that these distinctive near-periastron contributions can be used to differentiate between frame dragging by the black hole and external contributions, which are more likely to affect the pulsar's motion near the apoapsis (see also Angéilil & Saha 2014). Figure 5 illustrates such Lense-Thirring contributions to the pulsar timing residuals for a highly-eccentric ($e = 0.9$), wide ($P_b = 3$ yr) pulsar orbit. From Figure 5 it is already clear that, from a single periastron passage that is covered by a dense observing campaign, we can already infer relevant constraints on the Sgr A* spin. We will present more detailed conclusions in the subsection on mock data simulations below.

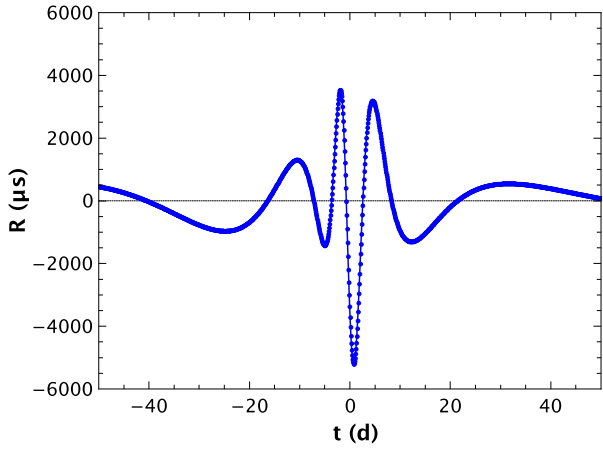


FIG. 5.— Timing residuals near periapsis passage ($t = 0$) for a pulsar in a highly eccentric ($e = 0.9$) 3 yr orbit around Sgr A*, when frame dragging effects have not been taken into account when fitting the pulsar orbit. We assume a Kerr spacetime with spin parameter $\chi = 0.6$. Concerning the orientation of the black hole, we used $\Theta = 60^\circ$, $\Upsilon_0 = \omega_0 = 45^\circ$, and $\lambda = 55^\circ$. The last value is motivated by Psaltis et al. (2015a). The dense timing campaign covers only one year around periapsis. Still, even after fitting the full DD model and allowing for a secular precession of the orbital plane, the frame-dragging (spin-orbit) contribution gives rise to a strong characteristic feature in the timing residuals.

4.2.1. Mock data simulations

While from the above discussion it is already obvious that the Lense-Thirring drag of the rotating black hole leads to a characteristic signal in the timing data, which ultimately allows the determination of the spin, we still need to address the question of spin measurement in a more quantitative way. For this reason, we have conducted extensive mock data simulations, based on the potential timing capabilities discussed in Section 2.3. The simulated TOAs were fitted with a timing model based on the equations of motion (41)–(45), that also include the relativistic effects discussed in Section 4.1. By this our simulations are based on a timing model that accounts for all the relevant effects to leading order. This model has been implemented in a timing software package, which is based on TEMPO and has been optimized for the timing analysis of Galactic Center pulsars. It allows for a fully phase-connected timing solution, providing a consistent parameter estimation. This is similar to the analysis presented in Liu et al. (2012); however, in addition, it properly accounts for the prominent near-periapsis features in the residuals, caused by the Lense-Thirring effect. As discussed above, this is of particular importance, if there are external perturbations to the pulsar orbit, moreover it also helps in determining the black hole spin on a shorter observing time-span, during which the second derivatives \ddot{x} and $\ddot{\omega}$ are not well measured. The latter is important in case the pulsar is only visible for a limited period of time, which will be the case for a pulsar at the Galactic Center, as discussed in § 2.3.

Figure 6 presents the measurement precision of the dimensionless spin parameter χ as a function of the observed number of periapsis passages for a pulsar in a 0.5 yr eccentric ($e = 0.8$) orbit. We have simulated a dense observing campaign where one obtains three precision TOAs per day. Simulations have been conducted for

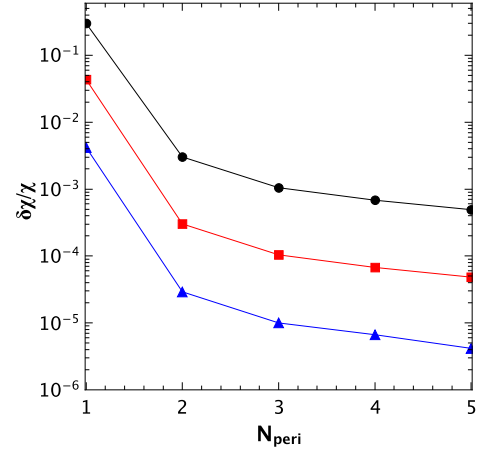


FIG. 6.— Fractional measurement precision ($2\text{-}\sigma$) for the spin parameter χ as a function of periapsis passages, based on a dense timing campaign. We have used the following values for the various parameters: $P_b = 0.5$ yr, $e = 0.8$, $\chi = 0.6$, $\sigma_{\text{TOA}} = 1$ μs (blue), 10 μs (red), 100 μs (black). The orientation of the spin is taken as in Figure 5. We assumed a daily timing campaign with three TOAs per session.

three different TOA uncertainties: 1, 10, and 100 μs , corresponding to our discussion in Section 2.3. As is evident from Figure 6, for all these TOA uncertainties we should be able to measure the spin of Sgr A* with very high precision, even if the observing time-span covers only a few periapsis passages. We have to keep in mind though, that the secular precession of the orbit, which is used in Figure 6 to determine the spin, also has a contribution from the quadrupole moment of the black hole. For a Kerr black hole and the orbits considered here, this contribution is considerably smaller than the spin contribution (cf. Figure 3). Nevertheless, for a 10^{-3} precision (or better) in the spin measurement within a no-hair-theorem test, we need to account for the quadrupole contribution without a priori assuming a fixed relation between spin and quadrupole moment.

As already argued in Wex & Kopeikin (1999) and demonstrated in detail in Liu et al. (2012), we have a good handle on the quadrupole from the characteristic periodic features in the timing residuals. In a consistent analysis we can, therefore, measure the quadrupole moment and simultaneously account for its contribution to the spin determination based on the secular precession of the pulsar orbit. Moreover, as we will discuss below in the subsection on the quadrupole measurement, the periodic residuals caused by the quadrupole moment have a signature that is quite different from the signature of the periodic spin contributions, which further helps to separate spin and quadrupole effects in the orbital motion.

In an ideal situation, the pulsar's motion around Sgr A* will only be affected by the gravitational field of the black hole, as we have assumed in the previous simulations. However, if the orbital motion of the pulsar is exposed to external perturbations, for instance by a nearby mass distribution due to stars or dark matter, then the orbit might show an additional precession, which a priori cannot be quantified (see Merritt et al. 2010 and discussion in § 2). This is expected to be of particular importance around apoapsis, where the pulsar spends most of its time, and where the gravitational effects from the

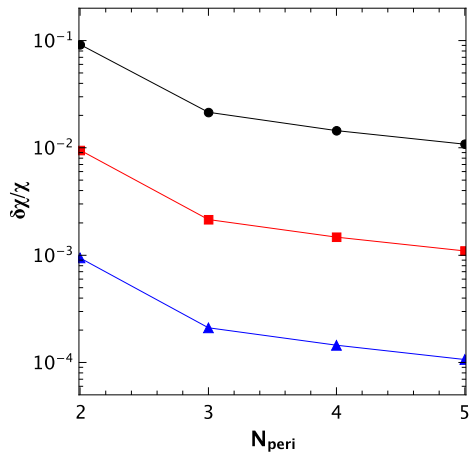


FIG. 7.— Fractional measurement precision ($2\text{-}\sigma$) for the spin parameter χ as a function of periastris passages for a pulsar orbit that suffers external perturbations and for which only TOAs near periastris can be used for parameter fitting (details in the text). The various parameters are similar to those in Figure 6.

black hole are weaker. In such a case, all the information on the black hole spin has to come from the expectedly dominating spin effects near the periastris. We have modeled such a situation in our simulations by taking only TOAs during the periastris passages (time interval of only $\pm 0.05 P$ around periastris). The estimated measurement precision for the spin of Sgr A* is plotted in Figure 7. While the measurement precision is weaker than in Figure 6, it is obvious that it will still be possible to measure the spin of Sgr A* with high precision just based on the characteristic Lense-Thirring signal near periastris (cf. Figure 5).

Finally, if we are only able to observe a single periastris passage, of a wide but highly eccentric orbit, like the one in Figure 5, a complete spin measurement might be out of range, due to the strong correlations with other timing parameters. Nevertheless, as our simulations show, we should still be able to get precise constraints on different spin-projections, like $\chi \cos \Theta$ and $\chi \sin \lambda$, similar to the situation in Liu et al. (2012), if for instance none of the higher derivatives in $\tilde{\omega}$ and x can be measured.

4.2.2. Determining the spatial orientation of the Sgr A* spin

Further constraints on the spin orientation, in particular on the direction of the projection of the spin into the plane of the sky, do come from the proper motion of Sgr A* with respect to the solar system barycenter (SSB). The transverse motion of Sgr A* with respect to the SSB modifies the observed Roemer delay by

$$\Delta_R^{\text{pm}} = \frac{1}{c} (\boldsymbol{\mu}^* \cdot \mathbf{r})(t - t_0), \quad (54)$$

where $\boldsymbol{\mu}^*$ is the angular proper motion vector of Sgr A* in the sky (Kopeikin 1996). The contribution Δ_R^{pm} has an impact on the arrival times of the pulsar signals which is distinctly different from Lense-Thirring contributions (see Fig. 8), and depends on the orientation of the pulsar orbit with respect to the well known proper motion of Sgr A* (Reid & Brunthaler 2004). This can be easily demonstrated by looking at the orbital averaged changes to the semi-major axis (x) and the longitude of periastris

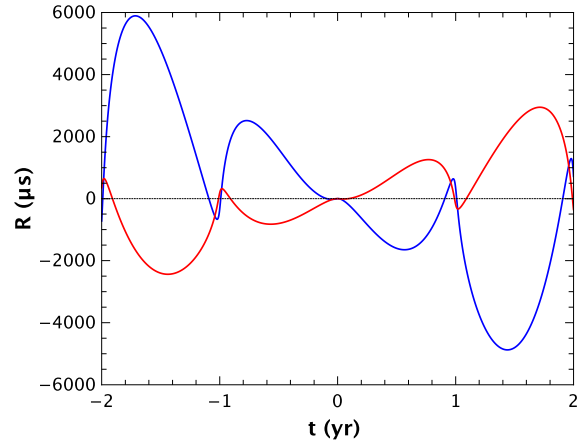


FIG. 8.— Contribution to the Roemer delay caused by the proper motion of Sgr A* with respect to the SSB, for a 1 yr orbit with an eccentricity $e = 0.8$. For the angles we have chosen $i = 60^\circ$, $\omega = 45^\circ$, and $\Omega = 0^\circ$ (blue) and 90° (red).

($\tilde{\omega}$), which are given by

$$\dot{x}/x = \mu^* \cot i \sin \Omega, \quad (55)$$

$$\dot{\tilde{\omega}} = -\mu^* \csc i \cos \Omega, \quad (56)$$

where Ω denotes the longitude of the ascending node (measured clockwise in the sky, with respect to the direction of proper $\boldsymbol{\mu}^*$). Hence, the proper motion contribution to the Roemer delay gives access to the sixth Keplerian parameter, i.e. Ω , and therefore completely determines the 3D orientation of the orbit. Consequently, since we know the orientation of the black hole spin with respect to the pulsar orbit from timing its orbital motion, the 3D orientation of the black hole spin can be determined. This is valuable input for combining pulsar observations with the measurements of the Sgr A* shadow with the EHT, as we will discuss in § 6.

4.3. Extracting the Quadrupole Moment From the Timing Residuals

Once the mass and spin are measured, a Kerr spacetime is fully determined. Consequently, as discussed above, the measurement of any higher multipole moment is a test of the Kerr hypothesis. For a pulsar in orbit around Sgr A* one can hope for the measurement of the quadrupole moment, as the leading multipole moment, after M_\bullet and S_\bullet . The quadrupole moment of Sgr A* leads to a distinct signal in the arrival times of the pulses, as it modifies the orbital motion of the pulsar in a characteristic way (Wex & Kopeikin 1999). Based on self-consistent mock data simulations, Liu et al. (2012) showed that, for a pulsar with an orbital period of a few months, it should be possible to extract the quadrupole of the Sgr A* spacetime from the timing residuals with high precision. Depending on the rotation of Sgr A* and the eccentricity of the orbit, this could be easily achieved with a precision of 1% or even better.

The simulations for the no-hair-theorem test in Liu et al. (2012) are based on the optimistic (cf. discussion in § 2) assumption that the pulsar orbit does not experience any relevant external perturbations and therefore the secular precession of the orbit can be used to de-

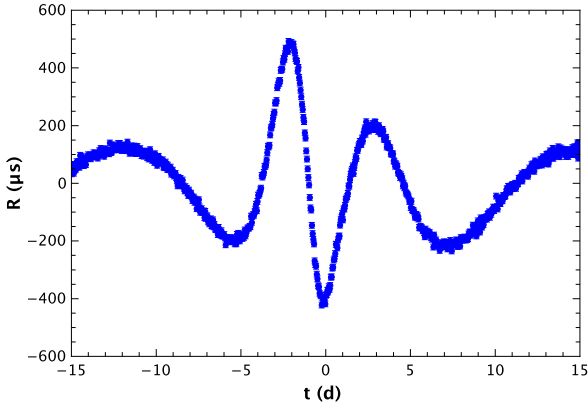


FIG. 9.— Signature of the black hole quadrupole moment, for an extreme Kerr black hole ($\chi = 1$). Simulations have been done for two periapsis passages, with the above figure zooming into the first one. $10 \mu\text{s}$ TOAs have been created only within ± 15 days around the periapsis passages for a pulsar in an eccentric ($e = 0.8$) orbit with $P_b = 0.5 \text{ yr}$. The orientation of the spin is taken as in Figure 5. The residuals are a result of a fit for the orbital and frame-dragging contributions. For demonstration purposes we have used a high timing cadence, to densely map the quadrupole signature. In practice, such a coverage would be the result of many periapsis-passage observations over a few years.

termine the spin of Sgr A*.⁴ In this section we relax this assumption, like we have done above for the spin measurement. For our simulations we added the implementation for the quadrupole moment of Liu et al. (2012) to our aforementioned extension of TEMPO. Figure 9 is the result of a simulation, where we use timing data only near periapsis, and allow for an undetermined overall precession of the orbit due to some unknown external perturbations. Figure 9 clearly shows that, after fitting for the pulsar spin parameters, orbital parameters, and frame dragging, there is still a distinctive signal in the residuals as a result of the quadrupole moment of the black hole. As a general result, depending on the timing-precision and the periapsis distance, we will still be able to extract the quadrupole moment of Sgr A*. Of course, this also depends on the actual value of the spin of Sgr A*, which is poorly constrained to date. In fact, the strength of the quadrupole effect scales with χ^2 , and is therefore clearly less prominent for a slowly rotating black hole (see Figure 10). Depending on the timing precision, however, the quadrupole moment can still be determined with high precision.

We have conducted extensive mock data simulations to study the joint measurability of spin and quadrupole moment. Like in the simulations for the spin measurement, we have assumed three TOAs per day. Figure 11 shows the timing coverage of the spin and quadrupole signature during one periapsis passage. Some of the results are illustrated in the contour plots of Figure 12. We conclude that, even for the conservative situation of a comparably low timing precision ($\sigma_{\text{TOA}} = 100 \mu\text{s}$) and the presence of external perturbations, a quantitative test of the Kerr hypothesis is possible after only a few periapsis passages. If we have a better timing precision or can make use of timing measurements along the whole orbit, the spin and

⁴ Liu et al. 2012 have demonstrated a way to identify the presence of external perturbations in the secular changes of the pulsar orbit.

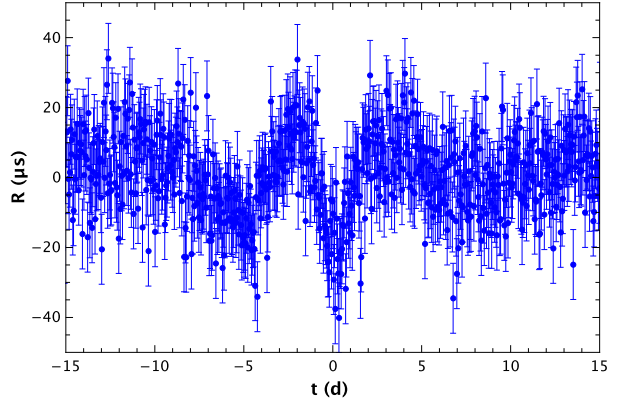


FIG. 10.— Same as in Figure 9, but this time with $\chi = 0.2$. In this case, the quadrupole moment of the black hole leads to a considerably less prominent signal in the residuals, but can still be measured accurately given the assumed TOA error of $10 \mu\text{s}$.

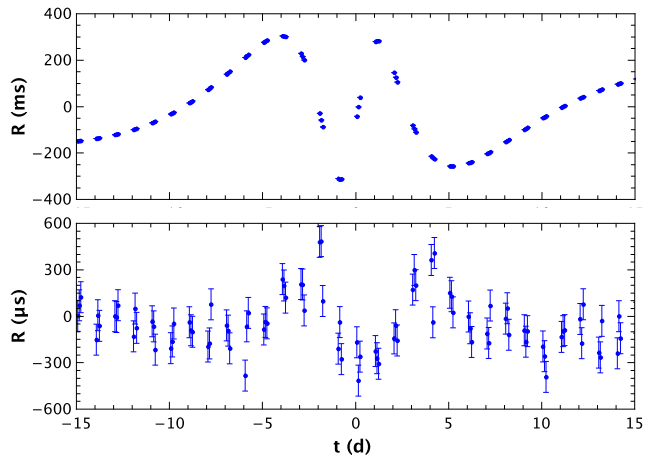


FIG. 11.— Mock-data TOA ($\sigma_{\text{TOA}} = 100 \mu\text{s}$) coverage of the spin (top) and quadrupole (bottom) signal during a periapsis passage. The simulated data cover three orbits. We used $\chi = 0.6$, $P = 0.5 \text{ yr}$, $e = 0.8$, $\Theta = 60^\circ$, $\Upsilon_0 = \omega_0 = 45^\circ$, and $\lambda = 55^\circ$.

quadrupole moment can be determined with high precision after a few orbits. The latter agrees with the findings in Liu et al. (2012).

4.4. Distance Measurement with Pulsar Timing

Given the large size of the pulsar orbit ($\sim 10^2 \text{ au}$), the orbital parallax (Kopeikin 1995), which is of order $\sim a^2/2cD$, will lead to a significant contribution to the timing observations, even for a moderate timing precision. This timing effect depends only on well determined orbital parameters and the distance to Sgr A*, D , and consequently can give independent access to D (cf. discussion in Subsection 4.1). The orbital parallax is a periodic signal in the timing residuals, and therefore, if we have N equally distributed TOAs with uncertainty σ_{TOA} , its measurement scales proportional to σ_{TOA} and \sqrt{N} . Consequently we find

$$\delta D \sim 2 \frac{c \sigma_{\text{TOA}}}{\sqrt{N}} \left(\frac{D}{a} \right)^2$$

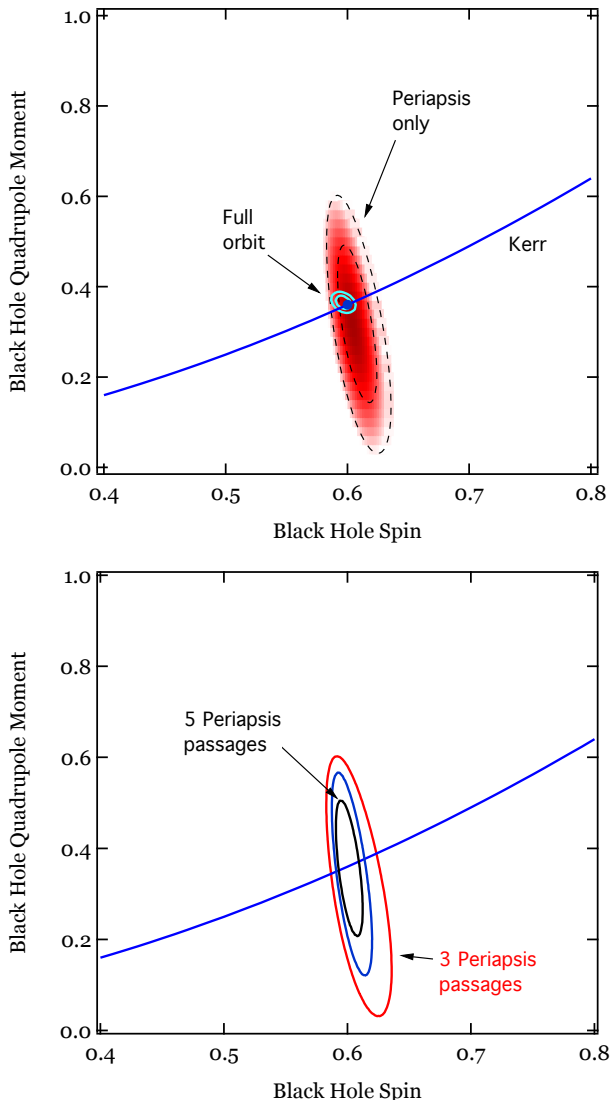


FIG. 12.— The posterior likelihood of measuring the spin and quadrupole moment of SgrA* using pulsar timing. In the top panel the dashed curves show the 68% and 95% confidence limits while, in the bottom panel, the solid curves show the 95% confidence limits. The solid curve shows the expected relation between these two quantities in the Kerr metric. The filled circle marks the assumed spin and quadrupole moment ($\chi = 0.6$, $|q| = 0.36$). The pulsar is assumed to have an orbital period of 0.5 yr (orbital separation of $2400 GM/c^2$) and an eccentricity of 0.8, while three TOAs per day with equal timing uncertainty of $100 \mu\text{s}$ have been simulated. The top panel compares the uncertainties in the measurement when only three periastron passages have been considered in the timing solution to those when the three full orbits are taken into account. The bottom panel shows the increase in the precision of the measurement when the number of periastron passages is increased from three to five.

$$\sim 20 \text{ pc} \left(\frac{\sigma_{\text{TOA}}}{10^2 \mu\text{s}} \right) \left(\frac{N}{10^3} \right)^{-1/2} \left(\frac{a}{10^2 \text{ au}} \right)^{-2}, \quad (57)$$

where we have used $D = 8.3 \text{ kpc}$.

External perturbations can also lead to changes of the orbit, which could in principle partly mimic the above effects. This, however, depends highly on the specifics of the perturbation, and we will not discuss this in further detail in this paper. On the other hand, as argued by Liu et al. (2012), a precise measurement of the SgrA*

mass from pulsar timing can be converted into a precise determination of the distance to SgrA*, when combined with high-precision astrometric observations in the infrared. For instance, a high precision measurement of M_\bullet in combination with the (angular) size of the S2-star orbit in Gillessen et al. (2009b) can be converted into a direct measurement of the Galactic center distance with an error of $\sim 100 \text{ pc}$. Future $10 \mu\text{s}$ astrometry promises a precision of order one parsec or even better.

5. PROBING THE SPACETIME OF SgrA* WITH THE EHT

The EHT will image the millimeter emission from SgrA* with horizon-scale resolution. There have been at least three proposals for using EHT observations to map the spacetime of this black hole and, in particular, to measure different combinations of its spin and quadrupole moment.

The first approach utilizes the detailed shape of the shadow cast by the black hole on the surrounding emission (Johannsen & Psaltis 2010b). Because of the combined effects of frame dragging and of the quadrupole deformation of the spacetime, the shadows of Kerr black holes are nearly circular, independent of the black-hole spin and the orientation of the observer (Bardeen 1973). The shadows of spacetimes that violate the no-hair theorem, however, can be significantly asymmetric, with the magnitude of asymmetry providing a measure of the degree of violation of relation (2); see Johannsen & Psaltis 2010b⁵. The shape of the shadow can be measured using the interferometric data either via an edge detection scheme (Psaltis et al. 2015a) or via fitting phenomenological geometric models (Ricarte & Dexter 2015).

In a second approach, simulated images of the accretion flow are fitted against the measured complex interferometric visibilities. The characteristic scale of the brightness in the accretion flow is set by the radius of the innermost stable circular orbit (see, e.g., Broderick et al. 2009; Dexter et al. 2010). For a general spacetime, this radius is determined, in turn, by a particular combination of the black-hole spin and quadrupole moment (see, e.g., Johannsen & Psaltis 2010a). Even the current, limited imaging data at 1.3 mm provide a glimpse of how this method can be used to constrain the properties of the black-hole spacetime by measuring the location of its innermost stable circular orbit (Broderick et al. 2014) and this technique will flourish as the full EHT array becomes operational.

Finally, if either GRAVITY or the EHT finds evidence for short-lived, compact emission regions (“hot spots”) that are advected with the accretion flow, tracing their orbits will lead to a measurement of the spacetime properties in a way that is similar to those discussed in §3 and §4 for orbits of stars and pulsars (Broderick & Loeb 2006; Vincent et al. 2011). The dynamical timescale in the vicinity of the horizon of SgrA* is equal to a few tens of minutes, i.e., much smaller than the time it will take

⁵ A number of studies have explored the shapes and sizes of black-hole shadows in modified gravity theories as well as in parametrically modified Kerr-like metrics (see, e.g., Bambi & Freese 2009; Bambi & Yoshida 2010; Johannsen 2012; Abdujabbarov et al. 2013; Amarilla & Eiroa 2013; Ghasemi-Nodehi et al. 2015). In this article, we focus on work that aims specifically to measure the quadrupole moment of the black-hole spacetime using its shadow properties.

to generate an image. As a result, tracing the orbits of such hot spots will be done by studying the time evolution of interferometric phases or closure phases along appropriate baselines and baseline triangles (Doeleman et al. 2009; Vincent et al. 2011).

All three approaches have the potential of measuring different combinations of the spin and quadrupole of the black hole. However, the first approach that involves measuring the shape of its shadow is purely gravitational and, as such, is the least model-dependent: it does not require a prior model of the accretion flow (as does the second technique) and does not rely on assumptions about the advection of particular compact emission regions along geodesics (as does the last technique). For this reason, we will focus here on the first approach as a proof of principle of our prospect of measuring the properties of the black-hole spacetime with EHT observations.

Johannsen & Psaltis (2010b) explored the asymmetry of the shadows of spacetimes with independent spins and quadrupole moments. They used the Glampedakis & Babak (2006) spacetime, which is a formal solution to the Einstein field equations up to the quadrupole order and remains regular only for relatively slow spins (see discussion in Johannsen 2013). They devised an approximate relation that connects the asymmetry of the shadow to the spin of the black hole, its quadrupole moment, and the inclination of the observer, i.e.,

$$A(\chi, q) = \left[0.84 (\chi^2 + q) + 0.36 \chi^3 \right] \left(\frac{GM_\bullet}{c^2} \right) \sin^{3/2} \lambda. \quad (58)$$

As this relation shows, when the no-hair theorem is satisfied, the asymmetry depends only the third power of the spin, with a small coefficient, becoming negligible for all but the fastest spinning black holes. Measuring any appreciable asymmetry of the black-hole shadow will be a strong evidence for a violation of the no-hair theorem.

The accuracy with which the shape of the black-hole shadow can be measured with EHT observations will depend on the particular techniques that will be used for image reconstruction and for pattern matching. Johannsen et al. (2012) used approximate relations for the flux of the photon ring that surrounds the black-hole shadow as well as an extrapolation of the demonstrated signal-to-noise ratio of existing EHT observations to infer that the radius of the shadow can be measured to an accuracy of

$$\sigma_{\text{rad}} \simeq 4.3 \left(\frac{1 \text{ mm}}{\lambda_{\text{obs}}} \right)^2 \left[\frac{53}{21} \left(\frac{1 \text{ mm}}{\lambda_{\text{obs}}} \right) - 1 \right]^{-1} \mu\text{as}, \quad (59)$$

where λ_{obs} is the observation wavelength. In the full EHT array, there are of order ~ 9 baselines with $u - v$ separations that are comparable to the position of the null due to the shadow and with locations that are nearly uniformly distributed around its circumference (see, e.g., Figure 3 of Ricarte & Dexter 2014). These separations will allow us to measure the overall asymmetry of the shadow along two axis with an accuracy of $\sigma_A \sim \sigma_{\text{rad}}/\sqrt{9} \simeq 0.9 \mu\text{as}$, where we evaluated this last expression at a wavelength of 1.3 mm. This estimate is in agreement with the detailed study of Ricarte & Dexter (2014), who used mock EHT observations to show that the quality of the data will allow measuring the

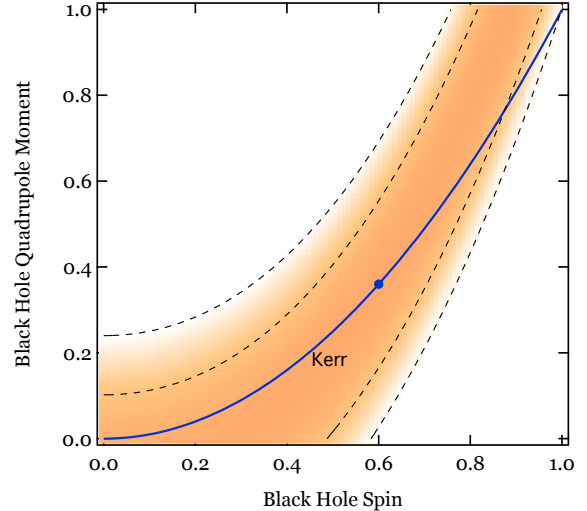


FIG. 13.— The posterior likelihood of measuring the spin and quadrupole moment of Sgr A* using EHT observations of the shape of its shadow. The dashed curves show the 68% and 95% confidence contours, while the solid curve shows the expected relation between these two quantities for the Kerr metric. The filled circle marks the assumed spin and quadrupole moment ($\chi = 0.6$, $|q| = 0.36$). As expected, the contours of maximum likelihood closely follow the Kerr relation, because any violation of the no hair theorem would have caused a measurable asymmetry in the shadow shape.

properties of asymmetric crescents to an accuracy that is smaller than a μas .

In order to visualize the correlated uncertainties in measuring the spin and quadrupole moment of Sgr A* using this technique, we will assume that EHT observations in the near future will lead to a measurement of the asymmetry of the shadow of a Kerr black hole with a spin $\chi = 0.6$, inclined at $\lambda = 55^\circ$ with respect to the observer. We will also assume a Gaussian posterior likelihood for this measurement, with a centroid given by equation (58) for $q = -\chi^2$, i.e., $A_0 = A(0.6, -0.36)$, and a dispersion equal to $\sigma_A = 0.9 \mu\text{as}$. Then, using Bayes' theorem, we can write the posterior likelihood that a given combination of a spin and quadrupole moment are consistent with the data as

$$P(\chi, q|\text{data}) = P(\text{data}|\chi, q)P(\chi)P(q), \quad (60)$$

where $P(\chi)$ and $P(q)$ are the priors over the spin and quadrupole, which we assume to be uniform between zero and one, and

$$P(\text{data}|\chi, q) = \frac{1}{\sqrt{2\pi\sigma_A^2}} \exp \left\{ -\frac{[A(\chi, q) - A_0]^2}{2\sigma_A^2 D^2} \right\}. \quad (61)$$

Figure 13 shows the resulting likelihood in the spin-quadrupole moment parameter space. As expected, the contours of maximum likelihood trace closely the Kerr relation $q = -\chi^2$, unless the black hole has a very high spin, because any violation of the no-hair theorem would have caused a measurable asymmetry in the shadow shape.

It is important to emphasize that we have only considered here, in an approximate fashion, the uncertainties related to the effective resolution of the EHT images. The uncertainty in our prior knowledge of the ratio GM/cD^2 does not enter this measurement, because what we will be measuring is the fractional asymmetry of the

shadow shape with respect to its overall apparent angular size. However, measuring the shape of the black-hole shadow at the $\simeq 1\%$ level requires a prior knowledge, at a comparable level, of the properties of the scattering screen that blurs the image. Our ability to characterize the scattering screen at longer wavelengths and extrapolate its properties down to the 1.3 mm wavelength of the EHT observations will be the main limiting factor in performing a test of the no-hair theorem with the EHT (see discussion in Fish et al. 2014; Psaltis et al. 2015a).

6. COMBINING THE EHT EXPERIMENT WITH STELLAR ORBITS AND PULSAR TIMING TESTS

In the previous sections, we discussed in detail the constraints on the measurement of the black-hole mass, spin, and quadrupole moment that will be achieved in the very near future with upcoming observations of stars, of pulsars, and of the black-hole shadow in Sgr A*. Even though each type of observation may lead by itself to a measurement of the black-hole properties, combining all three of them offers an unprecedented advantage for three reasons.

First, each of these measurements will probe the spacetime at very different distances from the black hole: pulsars and stars will probe hundreds to thousands of gravitational radii, and the Event Horizon Telescope will probe the inner tens of gravitational radii. If a significant amount of matter is hidden very close to the black hole in the form of dark matter particles or stellar-mass black holes, these three different probes will allow us not only to constrain the profiles of the hidden mass distribution but also to understand the biases it introduces to the measurement of the black-hole properties.

Second, each of the measurements uses a very different observational technique (e.g., astrometric positions of stars, timing of radio pulsars, sub-mm images of the accretion flow) and is, therefore, subject to very different systematic uncertainties. Comparing the results from the three types of observations will allow us to identify the systematics inherent to each.

Finally, each type of observations is expected to lead to correlated uncertainties (or even degeneracies) between the black-hole spin and quadrupole moment. However, the correlations and degeneracies in each method are along different directions in the parameter space (see Figure 14). The orbital precession of stars and pulsars will measure primarily the spin of the black hole. The timing of pulsars will measure independently the quadrupole moment of the spacetime. A detection of an asymmetry of the black-hole shadow will measure deviations of the quadrupole moment from the Kerr value. Combining all these measurement will lead to uncorrelated measurements of the black-hole spin and quadrupole moment and hence provide a test of the gravitational no-hair theorem.

Even though our focus in this article has been on testing the no-hair theorem, it is also important to emphasize that combining these three types of measurements will also have other important implications for the astrophysics of accretion flows and of supermassive black holes in the centers of galaxies. For example, as discussed above, differences among the enclosed mass inferred at

different radii with the EHT, with stars, and with pulsars, will allow us to constrain the distribution of stellar objects and dark matter at the very center of our Galaxy.

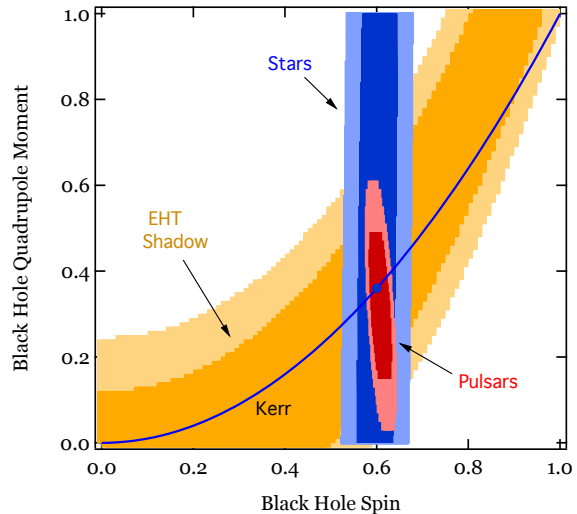


FIG. 14.— Comparison of the posterior likelihood of measuring the spin and quadrupole moment of Sgr A* using the orbits of two stars (*blue*), timing of three periaapsis passages of a low-precision pulsar (*red*), and the shape of its shadow (*gold*). The solid curve shows the expected relation between these two quantities for the Kerr metric. The filled circle marks the assumed spin and quadrupole moment ($\chi = 0.6$, $|q| = 0.36$). Combining these three independent types of measurements, each of which suffers from different biases and potential systematic uncertainties, will significantly increase our confidence in the inference of these two black-hole properties and in the test of the no-hair theorem.

Furthermore, measurement of the relative orientation of the black-hole spin and the angular momentum of the inner accretion flow will inform our understanding of black-hole feeding and alignment of black-hole spins (see, e.g., the discussion in Psaltis et al. 2015a).

It is true that the EHT and GRAVITY experiments still need to demonstrate that they can operate at their designed specifications and a pulsar, as well as at least two stars need to be discovered in sufficiently close orbits around Sgr A* for the three types of observations discussed here to be realized at the required accuracy. However, all these are possible in the very near future and promise to revolutionize our probes and understanding of strong-field gravity and accretion flows in the vicinity of black holes.

DP thanks the Max-Planck-Institut für Radioastronomie for their hospitality during the visit in which this project was conceived. DP acknowledges support from NASA/NSF TCAN award NNX14AB48G and NSF grant AST 131203. NW acknowledges valuable discussions with Tal Alexander and Kuo Liu. This work has been supported by the ERC Synergy Grant *BlackHole-Cam* under grant agreement no. 610058. This research was also supported by the Munich Institute for Astro- and Particle Physics (MIAPP) of the DFG cluster of excellence “Origin and Structure of the Universe”.

REFERENCES

- Angéil, R. & Saha, P. 2014, MNRAS, 444, 3780
- Angéil, R., Saha, P., & Merritt, D. 2010, ApJ, 720, 1303
- Bahcall, J. N., & Wolf, R. A. 1976, ApJ, 209, 214
- Bambi, C. & Freese, K. 2009, Phys. Rev. D, 79, 043002
- Bambi, C., & Yoshida, N. 2010, Classical and Quantum Gravity, 27, 205006
- Barausse, E., & Sotiriou, T. P. 2008, Physical Review Letters, 101, 099001
- Bardeen, J. M. 1973, in Black Holes, ed. C. DeWitt & B. S. DeWitt (New York: Gordon and Breach)
- Bates, S. D., Johnston, S., Lorimer, D. R., et al. 2011, MNRAS, 411, 1575
- Bower, G. C., Deller, A., Demorest, P., et al. 2014, ApJ, 780, L2
- Bower, G. C., Deller, A., Demorest, P., et al. 2015, ApJ, 798, L2
- Bramante, J. & Linden, T. 2014, Physical Review Letters, 113, 191301
- Broderick, A. E., Fish, V. L., Doeleman, S. S., & Loeb, A. 2009, ApJ, 697, 45
- Broderick, A. E., Fish, V. L., Doeleman, S. S., & Loeb, A. 2011, ApJ, 735, 110
- Broderick, A. E., Johannsen, T., Loeb, A., & Psaltis, D. 2014, ApJ, 784, 7
- Broderick, A. E. & Loeb, A. 2006, MNRAS, 367, 905
- Carter, B. 1971, Physical Review Letters, 26, 331
- Chan, C.-K., Psaltis, D., Özel, F., Narayan, R. & Sądowski, A. 2015, ApJ, 799, 1
- Chennamangalam, J. & Lorimer, D.R. 2014, MNRAS, 440, L86
- Cordes, J. M. & Lazio T. J. W. 2001, ApJL, 562, L157
- Cordes, J. M. & Lazio T. J. W. 2002, astro-ph/0207156
- Damour, T. & Deruelle, N. 1985, Ann. Inst. H. Poincaré (Physique Théorique), 43, 107
- Damour, T. & Deruelle, N. 1986, Ann. Inst. H. Poincaré (Physique Théorique), 44, 263
- Deneva, J. S., Cordes, J. M., Lazio, T. J. W. 2009, ApJ, 702, L177
- Dexter, J., Agol, E., Fragile, P. C., & McKinney, J. C. 2010, ApJ, 717, 1092
- Dexter, J. & O’Leary, R. M. 2014, ApJ, 783, L7
- Doeleman, S., Agol, E., Backer, D., et al. 2009a, astro2010: The Astronomy and Astrophysics Decadal Survey, 2010, 68
- Doeleman, S. S., Fish, V. L., Broderick, A. E., Loeb, A., & Rogers, A. E. E. 2009b, ApJ, 695, 59
- Eatough, R. P., Falcke, H., Karuppusamy, R., et al. 2013, Nature, 501, 391
- Eatough, R. P., Kramer, M., Klein, B., et al. 2013, in IAU Symposium 291, ed. van Leeuwen, CUP, 291, 382
- Eatough, R., Lazio, T. J. W., Casanellas, J., et al. 2015, in Advancing Astrophysics with the Square Kilometre Array (AASKA14), arXiv:1501.00281
- Einstein, A. 1915, Erklärung der Perihelbewegung des Merkur aus der allgemeinen Relativitätstheorie. *Sitzungsberichte der Königlich Preussischen Akademie der Wissenschaften (Berlin)*, 1915, pages 831–839.
- Eisenhauer, F., Perrin, G., Brandner, W., et al. 2011, The Messenger, 143, 16
- Falcke, H., Melia, F. & Agol, E. 2000, ApJ, 528, L13
- Faucher-Giguère, C.-A. & Loeb, A. 2011, MNRAS, 415, 3951
- Fish, V. L., Johnson, M. D., Lu, R.-S., et al. 2014, ApJ, 795, 134
- Genzel, R., Eisenhauer, F., & Gillessen, S. 2010, Reviews of Modern Physics, 82, 3121
- Ghasemi-Nodehi, M., Li, Z., & Bambi, C. 2015, The European Physical Journal C, 75, 9
- Ghez, A. M., Morris, M. R., Do, T., et al. 2012, Twelfth Marcel Grossmann Meeting on General Relativity, 420
- Ghez, A. M., Salim, S., Weinberg, N. N., et al. 2008, ApJ, 689, 1044
- Gillessen, S., Eisenhauer, F., Trippe, S., et al. 2009a, ApJ, 692, 1075
- Gillessen, S., Eisenhauer, F., Fritz, T. K., et al. 2009b, ApJ, 707, L114
- Glampedakis, K., & Babak, S. 2006, Classical and Quantum Gravity, 23, 4167
- Hansen, R. O. 1974, Journal of Mathematical Physics, 15, 46
- Hawking, S. W. 1972, Commun. Math. Phys., 25, 152
- Ho, L. C. 2008, ARA&A, 46, 475
- Hobbs, G. B., Edwards, R. T., & Manchester, R. N. 2006, MNRAS, 369, 655
- Israel, W. 1967, Physical Review, 164, 1776
- Israel, W. 1968, Commun. Math. Phys., 8, 245
- Johannsen, T. 2013, Phys. Rev. D, 88, 044002
- Johannsen, T., & Psaltis, D. 2010a, ApJ, 716, 187
- Johannsen, T., & Psaltis, D. 2010b, ApJ, 718, 446
- Johannsen, T., Psaltis, D., Gillessen, S., et al. 2012, ApJ, 758, 30
- Johnston, S., Kramer, M., Lorimer, D.R., et al. 2006, MNRAS, 373, L6
- Kennea, J. A., Burrows, D. N., Kouveliotou, C., et al. 2013, ApJ, 770, L24
- Kopeikin, S. 1995, ApJ, 439, L5
- Kopeikin, S. 1996, ApJ, 467, L93
- Kramer, M., Klein, B., Lorimer, D. R., et al. 2000, in “IAU Colloq. 177: Pulsar Astronomy - 2000 and Beyond”, eds. M. Kramer, N. Wex, & R. Wielebinski, ASPC, 202, 37
- Klein, B., Kramer, M., Müller, P., & Wielebinski, R. 2004, in IAU Symp. 218, Young Neutron Stars and Their Environments, ed. F. Camilo & B. M. Gaensler (San Francisco, CA: ASP), 133
- Lazarus, P., et al. 2015, ApJ, in press (arXiv:1504.02294)
- Liu, K., Wex, N., Kramer, M., Cordes, J. M., Lazio, T. J. W. 2012, ApJ, 747, 1
- Liu, K., Eatough, R. P., Wex, N., & Kramer, M. 2014, MNRAS, 445, 3115
- Löhmer, O., Kramer, M., Mitra, D., Lorimer, D. R., Lyne, A. G. 2001, ApJL, 562, L157
- Löhmer, O., Mitra, D., Gupta, Y., Kramer, M., Ahuja, A. 2004, A&A, 425, 569
- Lorimer, D. R. & Kramer, M. 2004, *Handbook of Pulsar Astronomy*. Cambridge University Press, Cambridge
- Lu, R.-S., Broderick, A. E., Baron, F., et al. 2014, ApJ, 788, 120
- Macquart, J.-P., Kanekar, N., Frail, D. A. & Ransom S. M. 2010, ApJ, 715, 939
- Macquart, J.-P. & Kanekar, N. 2015, ApJ, 805, 172
- Merritt, D. 2010, ApJ, 718, 739
- Merritt, D., Alexander, T., Mikkola, S., & Will, C. M. 2010, Phys. Rev. D, 81, 062002
- Meyer, L., Ghez, A. M., Schödel, R., et al. 2012, Science, 338, 84
- Mori, K., Gotthelf, E. V., Zhang, S., et al. 2013, ApJ, 770, L23
- Narayan, R. & McClintock, J. E. 2013, arXiv:1312.6698
- O’Leary, R. M., Kistler, M. D., Kerr, M., Dexter, J. 2015, arXiv/1504.02477
- Olausen, S. A. & Kaspi, V. M. 2014, ApJS, 212, 6
- Olausen, S. A. & Kaspi, V. M. 2014, ApJS, 212, 6
- Özel, F., Psaltis, D., Narayan, R., & McClintock, J. E. 2010, ApJ, 725, 1918
- Penrose, R., 1979, in S. W. Hawking & W. Israel, ed., General Relativity: An Einstein centenary survey, Vol. 1. Cambridge; New York: Cambridge University Press, p. 581
- Pfahl, E. & Loeb, A. 2004, ApJ, 615, 253
- Price, R. H. 1972a, Physical Review D, 5, 2419
- Price, R. H. 1972b, Physical Review D, 5, 2439
- Psaltis, D. 2012, ApJ, 759, 130
- Psaltis, D. & Johannsen, T. 2011, Journal of Physics Conference Series, 283, 012030
- Psaltis, D., Li, G., & Loeb, A. 2013, ApJ, 777, 57
- Psaltis, D., Narayan, R., Fish, V. L., Broderick, A. E., Loeb, A., Doeleman, S. S., 2015a, ApJ, 798, 15
- Psaltis, D., Özel, F., Chan, C.-K., & Marrone, D. P. 2015b, ApJ, submitted, arXiv:1411.1454
- Psaltis, D., Perrodin, D., Dienes, K. R., & Mocioiu, I. 2008, Physical Review Letters, 100, 1101
- Reid, M. J. & Brunthaler, A., 2004, ApJ, 616, 872
- Reid, M. J., Menten, K. M., Brunthaler, A., et al. 2014, ApJ, 783, 130
- Ricarte, A., & Dexter, J. 2015, MNRAS, 446, 1973
- Robinson, D. C. 1975, Physical Review Letters, 34, 905
- Ryan, F. D. 1995, Physical Review D, 52, 5707
- Sadeghian, L. & Will, C. M. 2011, Classical and Quantum Gravity, 28, 225029
- Shannon, R. M. & Johnston, S. 2013, MNRAS, 435, L29
- Siemion, A., Bailes, M., Bower, G., et al. 2013, in IAU Symposium 291, ed. van Leeuwen, CUP, 291, 57
- Spitler, L. G., Lee, K. J., Eatough, R. P., et al., 2014, ApJ, 780, L3
- Sotiriou, T. P. & Faraoni, V. 2012, Physical Review Letters, 108, 081103

- Thorne, K. S. 1980, *Reviews of Modern Physics*, 52, 299
- Torne, P., Eatough, R. P., Karuppusamy, R., et al. 2015, *MNRAS*, 451, L50
- Vincent, F. H., Paumard, T., Perrin, G., et al. 2011, *MNRAS*, 412, 2653
- Weinberg, N. N., Milosavljević, M., & Ghez, A. M. 2005, *ApJ*, 622, 878
- Wex, N. 1995, *Classical and Quantum Gravity*, 12, 983
- Wex, N. & Kopeikin, S. 1999, *ApJ*, 513, 388
- Will, C. M. 2008, *ApJ*, 674, L25
- Wharton R. S., Chatterjee, S., Cordes, J. M., et al. 2012, *ApJ*, 753, 108